

# Deep Wavefront Shaping: Intelligent Control of Complex Scattering Responses with a Programmable Metasurface

Benjamin W. Frazier,<sup>1,2,3,\*</sup> Thomas M. Antonsen, Jr.,<sup>1,2,4</sup> Steven M. Anlage,<sup>2,4,5</sup> and Edward Ott<sup>1,2,4</sup>

<sup>1</sup>*Institute for Research in Electronics and Applied Physics,  
University of Maryland, College Park, MD 20742, USA*

<sup>2</sup>*Department of Electrical and Computer Engineering,  
University of Maryland, College Park, MD 20742, USA*

<sup>3</sup>*Johns Hopkins University Applied Physics Laboratory, Laurel, MD 20723, USA*

<sup>4</sup>*Department of Physics, University of Maryland, College Park, MD 20742, USA*

<sup>5</sup>*Quantum Materials Center, University of Maryland, College Park, MD 20742, USA*

(Dated: March 1, 2025)

Electromagnetic environments are becoming increasingly complex and congested, creating a growing challenge for systems that rely on electromagnetic waves for communication, sensing, or imaging. The use of intelligent, reconfigurable metasurfaces provides a potential means for achieving a radio environment that is capable of directing propagating waves to optimize wireless channels on-demand, ensuring reliable operation and protecting sensitive electronic components. Here we introduce “deep wavefront shaping”, a technique that combines a deep learning network with a binary programmable metasurface to shape waves in complex electromagnetic environments and to drive the system towards a desired scattering response. We applied this technique to accurately determine metasurface configurations based on measured system scattering responses in a chaotic microwave cavity. The state of the metasurface that realizes desired electromagnetic wave field distribution properties was successfully determined even in cases previously unseen by the deep learning algorithm. Our work represents an important step towards realizing intelligent reconfigurable metasurfaces for smart radio environments that can ensure both the integrity of electronic systems and optimum performance of wireless networks.

## I. INTRODUCTION

Highly scattering environments scramble electromagnetic waves, producing interference among the multiple paths between source and receiver. The resulting spatio-temporal fluctuations can seriously degrade imaging, sensing, and communication systems at microwave and optical wavelengths, disrupting operation or even damaging sensitive components. Large enclosed spaces, such as offices or compartments on ships or aircraft can act as “chaotic” reverberating chambers for short-wavelength electromagnetic waves [1]. Additional emissions in these environments, whether from unintentional coupling between components or from an intentional electromagnetic attack, can have serious consequences. Future smart radio environments are envisioned to handle such dynamic conditions, adapting on-the-fly to optimize a given wireless channel [2, 3]; e.g. this optimization includes the ability to generate coldspots to protect sensitive electronic devices and realize coherent perfect absorption states for long range wireless power transfer. Intelligently controlling wave fields in the presence of multi-path reflections is therefore a critical factor for enabling smart radio environments. In addition, an intelligent and self-adaptive approach will benefit applications such as micromanipulation of objects in complex scattering environments [4], and time reversal mirrors that can

selectively focus a wavefront or enhance communication system performance [5, 6].

In optics, spatial light modulators have been used to control waves under strong scattering conditions for some time. Applications range from focusing through general disordered media [7, 8] to sophisticated biomedical imaging instruments that fall under the umbrella of adaptive optics [9, 10]. In the last several years, spatial microwave modulators in the form of programmable metasurfaces have also become widely available. Programmable electromagnetic metasurfaces are metamaterial sheets that can modify their local surface impedance over unit cells (meta-atoms) that have a sub-wavelength characteristic size. They have emerged as powerful tools for shaping waves inside complex microwave cavities [11–19].

Metasurfaces are not limited to shaping only electromagnetic waves. In seismology, control over surface acoustic waves has been demonstrated using metasurfaces made of elastic metamaterials for Love waves (horizontally polarized) [20] and Rayleigh waves (containing both longitudinal and transverse motion) [21]. In the case of quantum waves, a metasurface created from an array of trapped neutral atoms was used to manipulate light at the quantum level [22]. While the underlying physics of these metasurfaces is vastly different, the overall operation and process of wave interaction is essentially the same, implying that strategies for wavefront shaping in one domain can be readily adapted to another.

In this work, we use a binary programmable metasurface to shape radio frequency electromagnetic waves inside a chaotic microwave cavity, and present a deep learn-

---

\* Benjamin.Frazier@jhuapl.edu

ing network capable of determining the configuration of the metasurface that accurately produces a given scattering response. The deep learning network is trained and tested on measured frequency dependent  $S_{21}$  parameters and achieves accuracy of the desired response exceeding 95%. This high success rate is achieved with a limited amount of training data, requiring the collection of far fewer sets than the number of possible combinations of metasurface commands. Training is performed in a parallelized fashion over all the training data at once, e.g., for our computational resources, taking  $\sim 4$  hours to collect a sufficient set of data and train the deep learning network. Testing, however, is performed on single shot measurements and takes less than 1 second to measure the  $S_{21}$  response and make a determination of the metasurface commands, enabling real-time operation.

Our technique, which we call “deep wavefront shaping” is achieved through the development and combination of four major novel aspects: 1) Adaptive configuration of the metasurface unit cells by binning elements together to dynamically alter the relative size of the elements; 2) Representation of the complex system  $S$ -parameters in a pseudo-2D “image” to promote extraction of features that are correlated over both local and global frequencies; 3) Complex-valued deep learning layers to exploit both phase and amplitude information, accelerating training and improving the accuracy when applied to complex scattering environments; and 4) Introduction of the Terrapin module to parallelize the deep learning network, promoting sparse feature representation and improving training robustness.

The rest of this paper is laid out as follows. Section II introduces the concept of deep wavefront shaping and examines the difficulties inherent in a complex scattering environment. Section III provides the experimental configuration, discussing the chaotic cavity and metasurface along with the approaches taken for binning the metasurface pixels and preparing the data for the deep learning network. Section IV discusses the design of the deep learning network, introducing the use of complex-valued layers and the “Terrapin” module. Section V presents the results observed during training of the deep learning network and the subsequent closed loop validation. Finally, Section VI provides a summary and discusses the ramifications and future directions for our deep wavefront shaping paradigm.

## II. DEEP WAVEFRONT SHAPING

Microwave experiments have shown that programmable metasurfaces can provide fine control over the scattering parameters of a cavity, with the most recent work demonstrating perfect absorption [16] and coherent perfect absorption [18, 19] states inside the cavity. The relationship between metasurface commands and cavity scattering parameter responses is extremely complicated (there are  $10^{72}$  possible configurations of

the metasurface in our case, as will be discussed later). Therefore, optimization of the metasurface is typically handled through brute force trial and error or stochastic search algorithms [18, 23, 24]. However, the inherent complexity of this configuration makes it an ideal place to utilize deep learning. Ma et al. explored the use of deep learning networks with wave chaotic systems, demonstrating the ability to successfully distinguish between different types of wave chaotic cavities through the measured  $S$ -parameters [25]. We now tackle a more difficult problem, quickly identifying a set of metasurface commands required to achieve a specific wave scattering requirement, even for cases where that set of commands has not been previously encountered.

Since 2018, deep learning has been successfully used to design metasurfaces for wavefront shaping applications in both the photonic and microwave domains [26–36]. However, most of the publications so far have focused on designing and arranging the individual unit cells of the metasurface for static use cases. For microwave imaging applications, deep learning networks have been used with a programmable metasurface [37–41]; however, the metasurface is used simply to establish phase diversity and is decoupled from the deep learning network. Li et al. used a two-bit coding metasurface to generate radiation patterns for a machine learning algorithm that detects and classifies human movement [37, 38]. del Hougne et al. started with a pair of metasurfaces as a transmitter and receiver to feed a dense neural network that detects and classifies objects in a learned integrated sensing paradigm [39]. Further research by this group used a dense neural network to classify the position of a scattering object inside a complex cavity with a metasurface acting as a coded aperture [40]; this work was recently extended to predict a continuous position with sub-wavelength precision [41]. These examples demonstrate how a programmable metasurface can enhance the processing power of a deep learning network for microwave imaging, but they do not leverage the deep learning network for active control of the metasurface.

Active control, where the deep learning network is used to program the metasurface, is a key component of intelligent wavefront shaping. This has so far been an under-explored area of research. Qian et al. used a simple dense network to enable cloaking of an object [42], while Shan et al. used a 2D convolutional network to optimize the steering of multiple beams [43]. Both cases utilize an idealized testing environment inside an anechoic chamber, where multi-path reflections from the environment are intentionally excluded. In addition, both cases are built around a propagation path with a direct reflection off the metasurface, which means that the metasurface interacts with virtually all ray trajectories from the source to the receiver.

When the metasurface is placed inside the scattering volume [40, 41], determining the relationship between metasurface commands and scattering responses becomes substantially more difficult due to the presence of multi-

ple scattering paths. The limited physical extent of the metasurface relative to the volume means many ray trajectories do not interact with the metasurface, providing an additional complication. The difficulty is further compounded as we wish to optimize the metasurface response over a wide bandwidth or even over multiple separated bandwidths simultaneously.

In this paper we show that the inclusion of deep learning provides for an intelligent reconfigurable metasurface, which can be used to intelligently shape electromagnetic waves in a complex scattering environment. A conceptual view of this technique, referred to as “deep wavefront shaping”, is given in Fig. 1. The metasurface is placed in a complicated scattering environment, with a signal injected at Port 1 and the resulting field measured at a specific point of interest (Port 2). The environment is defined by irregular walls and inclusions and is probed by waves with wavelengths much smaller than the characteristic dimension of the enclosure. The deep learning network can adapt and dynamically learn on-the-fly to optimize the metasurface commands under changing environmental conditions or port locations. We anticipate that realization of this concept will help usher in the new era of smart radio environments [2, 3], as well as allow on-demand creation of coherent perfect absorption states for long range wireless power transfer or microwave cold spots to protect sensitive electronic components.

This work demonstrates that a deep learning network can exploit the complicated relationship between cavity scattering parameters and metasurface commands when the metasurface is placed inside a chaotic microwave cavity. We further show that the trained network can successfully determine the metasurface configuration from the measured scattering response in the cavity several days after the training data was collected. Measured  $S_{21}$  responses with the same initial conditions inside a chaotic cavity will diverge over time, a phenomenon known as scattering fidelity decay [44–46]. This decay means that any deep learning system that learns scattering responses inside a chaotic cavity will require periodic retraining. As discussed in Section VI, the fact that we are still able to determine the metasurface configuration accurately after several days means our technique is operationally useful, as it can function at a high level of accuracy for a long period of time before requiring retraining. Our approach is robust and highly accurate in determining metasurface commands from measured cavity  $S_{21}$  spectra, providing an enabling capability for intelligent wavefront shaping applications.

Future efforts will refine deep wavefront shaping as a technique for intentionally scrambling (or unscrambling) waves propagating through a complex scattering environment. Three aspirational goals include: 1) Tuning the scattering responses through a controller that optimizes the system for a given application at arbitrary frequencies and bandwidths. Specific metrics include minimizing transmitted power for coldspot generation, minimizing scattering matrix eigenvalue magnitudes for coherent

perfect absorption, or minimizing the bit error rate for wireless communication; 2) Introducing feedback from the environment to dynamically update the controller and react to changing environmental conditions; and 3) Realizing a fully autonomous systems that enables persistent and robust smart radio environments that do not require human intervention.

### III. CONFIGURATION

The complex, ray chaotic cavity used for experimentation has a binary programmable metasurface installed on an interior wall. It has a volume of  $0.74 \text{ m}^3$  and is in the same configuration used in our previous work [18], as discussed in Section S1 and Fig. S1 of the supplemental material. The metasurface was fabricated by the Johns Hopkins University Applied Physics Laboratory and is designed to operate in the frequency range of 3-4 GHz. It contains 240 binary meta-atoms arranged in a rectangular grid of  $10 \times 24$  elements. Each element has a characteristic length of  $\sim \lambda/6$  and is switched by a GaAs transistor amplifier to 1 of 2 states (0 or 1), changing the phase of the reflection coefficient by  $\sim 180^\circ$  [47]. The metasurface covers a small region of the interior surface area of the cavity, 1.5%, so only a limited number of rays are intercepted by the metasurface.

The goal of our deep learning network is to accept a given  $S_{21}$  spectra from 3-4 GHz and accurately determine the metasurface commands necessary to closely realize that specific scattering response, effectively solving an inverse problem as described in Section S2 of the supplemental material. The relatively small size of the metasurface and its unit cells leads to high correlation between system scattering responses with minor changes in metasurface commands, which means the inverse problem is ill-posed. Deng et al. recently introduced a neural-adjoint approach for solving the ill-posed inverse problem of designing unit cell geometries to match specified absorption spectra [48]. In this case, a fully connected deep learning network was used to model the forward problem, acting as a Green’s function to predict the spectra from a given design. The inverse problem was then solved iteratively, driving the design along an estimated gradient towards the optimal solution. Gradient methods work best for a continuous or near continuous solution space rather than a binary one such as ours; however, the adjoint method from [48] can be adapted into a reinforcement learning approach as discussed in Section VI. In addition, inside a chaotic reverberating environment, the spectra will have more structure, resulting in higher frequency oscillations or local features that must also be learned. Therefore, we also require a different deep learning approach.

The complexity of the cavity scattering responses combined with the enormous number of possible metasurface command configurations ( $2^{240}$ ) means the direct development of a deep learning network for the full space of

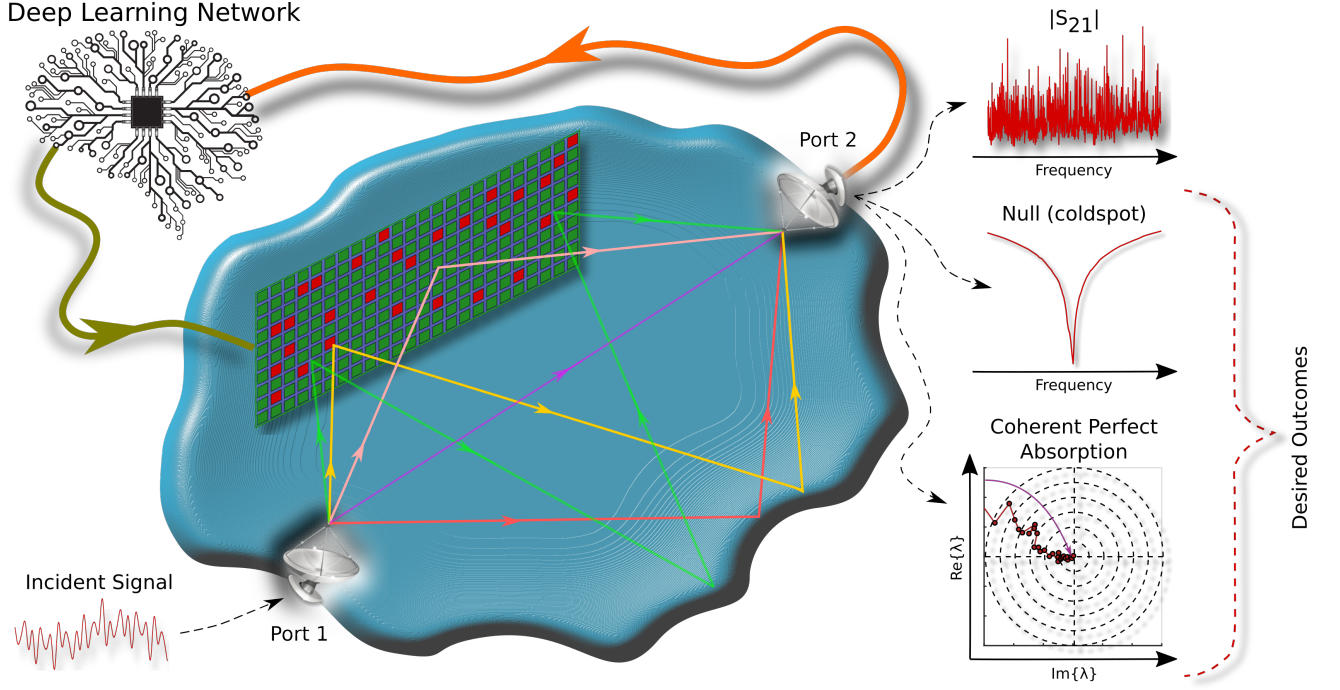


Figure 1. **Deep wavefront shaping conceptual overview.** Constructive and destructive interference between multiple propagation paths induces randomness in the scattering parameters and scrambles electromagnetic waves that are injected at Port 1. A reconfigurable metasurface is used to tune the interference to create cold spots for protection of sensitive electronic components, realize coherent perfect absorption states for long range wireless power transfer, or unscramble the output fields to enable smart radio environments. The metasurface, along with a sensing antenna at Port 2, is coupled with a deep learning network that provides intelligence. Measurements are used as training data, enabling the network to determine the control settings of the metasurface, and allowing the system to adapt to changing environmental conditions on-the-fly.

240 elements is overly ambitious. To simplify the problem, we reduced the number of degrees of freedom of the metasurface by binning together neighboring pixel elements, or grouping them together so that each element in a group is always commanded with the same value. Binning the metasurface elements reduces the total number of elements that must be determined and strengthens the relative change in cavity scattering parameters when driving a single effective element. Binning also promotes generality, as a metasurface with smaller elements can always approximate one with larger elements. This provides the first major novel aspect of our approach and allows us to explore the use of deep learning models in simpler configurations before working our way up to the more difficult cases.

We used 4 different metasurface binning configurations, as shown in Fig. 2, to progressively decrease the number of elements. With no binning, there are 240 elements arranged in a  $10 \times 24$  grid, which allows  $1.8 \times 10^{72}$  possible combinations of commands. Binning elements into  $2 \times 2$  groups results in 60 elements in a  $5 \times 12$  grid and  $1.2 \times 10^{18}$  possible combinations, while binning elements into  $3 \times 3$  groups results in 24 elements in a  $3 \times 8$  grid and  $1.7 \times 10^7$  possible combinations. In the  $3 \times 3$  binning configuration, the bottom row consists of  $4 \times 3$  groups to ensure all the elements are included. Finally,

binning elements into  $5 \times 4$  groups results in 12 elements in a  $2 \times 6$  grid and 4096 possible combinations.

An important step for deep learning is preparation of the measured data. The raw data consists of  $M$  sets of complex two-port  $S$ -parameter values, each containing 32,001 points measured over a 3-4 GHz window. We are interested in the relationship between metasurface commands and transmission between the ports, so we select  $S_{21}$  as the primary variable of interest. The measured data contains local and global correlations, both of which must be captured by the deep learning network. We can exploit the local correlations with 1D convolutional neural network (CNN) layers, but would like the individual windows to cover a smaller bandwidth. Our previous work showed diminishing returns for optimization over bandwidths greater than 10 MHz [18], so 10 MHz provides a reasonable limit for the local window size. We therefore extract the complex  $S_{21}$  in 10 MHz frequency windows at 100 distributed center frequencies to provide 100 feature vectors containing 321 points each. A representative data set is shown in Fig. 3 (a), with only 50 feature vectors used for illustration. The data are organized into a 3D structure of  $M$  sets of data  $\times F$  local frequencies  $\times N$  features, or  $10,000 \times 321 \times 100$  for the  $2 \times 2$  binning configuration. Each data set takes on a pseudo-2D format with a  $321 \times 100$  pixel “image” as



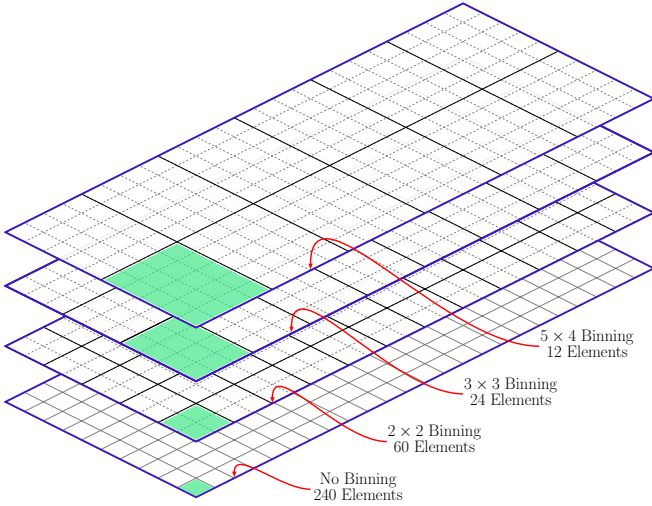


Figure 2. **Metasurface binning configurations.** Binning configurations showing the relationship between the various options. The shaded green region identifies a single effective element for the specified configuration and the thin gray lines show the layout of the unbinned elements. With no binning, there are 240 elements, binning into groups of  $2 \times 2$  yields 60 elements, binning into groups of  $3 \times 3$  yields 24 elements, and binning into groups of  $5 \times 4$  yields 12 elements. For the  $3 \times 3$  binning case, the bottom row of elements consists of a  $4 \times 3$  group so that all the elements are utilized.

shown in Fig. 3 (b). Local features in the 10 MHz frequency windows (over the  $F$  dimension) will be extracted by 1D CNN layers and global features (over the  $N$  dimension) will be extracted by the overall deep learning network architecture. The overall architecture then acts as a dense or fully connected layer from the perspective of the global features. The pseudo-2D format and its ability to capture both long-range and short-range correlations in frequency provides the second major novel aspect of our approach. A discussion of the different types of neural network layers used, and the general architecture for sequential layers, is provided in Sections S3, S4, S5, and S6 of the supplemental material.

The output values of the deep learning network (equal in number to the number of binned metasurface elements) are floating point numbers rather than binary numbers and can be interpreted as the probability that a given element in the metasurface is active (set to 1). The determined commands are then found by rounding the outputs to either a 1 or a 0. Inspection of the raw (unrounded) outputs allows us to assess how correct the deep learning network was, or how confident the network was in the result. Details of the network training approach are provided in Section S7 of the supplemental material.

A major concern with deep learning is the amount of data required for training, which grows with the complexity of the problem being solved. To work within the constraint of reasonable training time, we wish to limit the number of data sets that must be collected. Therefore,

acquiring good training data is of critical importance to ensure we cover the full range of possible responses. As found in earlier work [18], a diverse set of measurements requires variations in the number of active elements, spatial frequencies of active elements, and local groupings of active elements. Therefore, we utilized a random biased coin toss approach with the bias itself a uniformly distributed random number to assign values to the elements for training data generation. To speed up operation as much as possible, the microwave network analyzer was configured to only provide  $S_{21}$  measurements vs. frequency. With averaging disabled, collecting 4,000 sets of data took a little under an hour and a half, while collecting 10,000 sets of data took roughly 3.5 hours. Training was performed on a computer running Ubuntu 20.04 equipped with an NVIDIA RTX 3080 GPU.

The primary limitation of our approach is that we are not guaranteed to be able to generate any arbitrary  $S_{21}$  response, as a configuration of the metasurface that produces that response does not necessarily exist. The small size of the metasurface relative to the cavity limits its ability to interact with all possible ray trajectories, emphasizing the importance of a binning capability to adapt the effective pixel size to the environment. The small relative size of the metasurface does represent a realistic configuration for practical smart radio environments, however. In addition, real world chaotic systems contain short orbits, or prompt direct paths that do not ergodically sample the enclosure [49, 50]. Short orbits are persistent and manifest as correlations between realizations. Our method is general enough to operate under these conditions and does not require a specifically engineered environment.

#### IV. DEEP LEARNING NETWORK DESIGN

For the initial experiment, we collected 4000 sets of data in each of the specified binning configurations; the  $5 \times 4$  configuration allows 4096 unique metasurface combinations, so we collected 4096 sets (covering all possible combinations) in that case. With the exception of the  $5 \times 4$  binning configuration, the number of sets collected was far smaller than the number of possible configurations of the metasurface. The goal was to design a deep learning network that provided the best performance for the inverse problem; determining metasurface commands that approximately realize the desired complex transmission coefficient,  $S_{21}$  vs. frequency (3-4 GHz). Identifying the optimal deep learning network topology for a given binning configuration took a significant amount of time to iterate over many potential designs, e.g., for our computing resources, often several weeks, and was performed off-line. Once the deep learning network architecture was determined, we switched to an on-line, closed loop configuration where the data collection and training processes were separated by a few hours rather than days or weeks. The determined metasurface commands were directly ap-

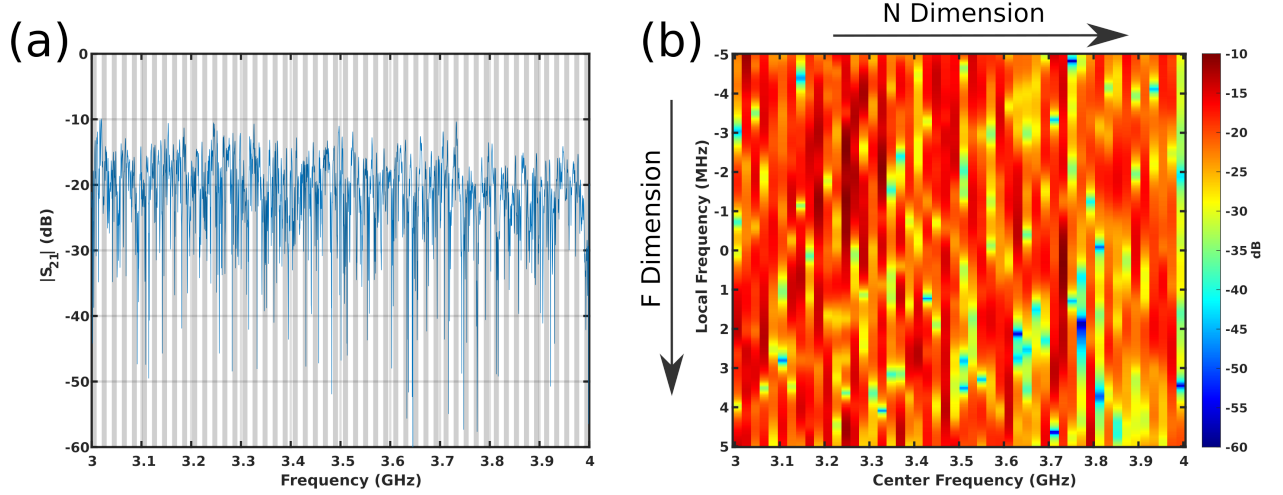


Figure 3. **Data preparation example.** The deep learning networks use complex amplitudes, however, only the magnitude is shown here for illustrative purposes. **(a)** Raw  $|S_{21}|$  data vs. frequency showing 50 local windows highlighted in gray. The actual data preparation uses 100 local windows, only 50 are shown here for clarity. The data was collected over a 1 GHz measurement window with 32,001 points and each local window (highlighted in gray) has a bandwidth of 10 MHz or 321 points. **(b)** Extracted  $|S_{21}|$  data (in log scale) in a pseudo-2D format as a  $321 \times 50$  pixel “image”. The data is represented as center frequency (over the full 1 GHz measurement window or  $N$  dimension) vs. local frequency (over the 10 MHz local window or  $F$  dimension). The deep learning network will use 1D convolutions to extract features in the 10 MHz local frequency windows ( $y$ -axis) and use the relationships between convolutional filters to capture global correlations over the full 1 GHz measurement window ( $x$ -axis).

plied to the metasurface and the resulting  $S_{21}$  responses were measured by the network analyzer, closing the loop. The on-line configuration also serves as a “field-test” for the deep learning network, further validating it against data not seen during training, as well as testing performance against potential small variations in measurement noise and the scattering configuration of the cavity itself.

The added complexity resulting from placing the metasurface inside a chaotic cavity requires a correspondingly complicated deep learning network to extract the relevant features. Rather than only designing progressively more intricate network topologies, we can also introduce complex-valued layers [51], which serve as the third major novel aspect of our approach. The wave scattering phenomenon is fundamentally complex-valued, so using complex-valued layers allows the network to better match the underlying physical system and exploit both phase and amplitude information. Complex-valued multiplicative layers have been used in this sense to invert propagation through multi-mode fibers [52, 53]. Unfortunately, as discussed in Section S5 of the supplemental material, there are no officially supported complex-valued modules in any of the major deep learning frameworks. Multiplicative layers are straightforward to implement, but more complicated modules, such as convolutional layers, are not. For the research described here, we leveraged the open source complexPyTorch library [54] as the basis for our complex-valued network layers.

As discussed in Section S8 of the supplemental material, we found that complex-valued layers required

fewer training epochs to converge, and generally provided more accurate solutions than purely real-valued layers. The acceleration in training comes with a caveat in that the overall computational time for the purely real-valued deep learning network is still less than that of the complex-valued deep learning network. Complex-valued layers increase the computation requirements for multiplication and convolution by a factor of 4 to handle the real and imaginary terms as well as the cross-terms. In addition, highly optimized and efficient implementations of purely real-valued layers are readily available through the NVIDIA CUDA deep neural network library (cuDNN), but are not available for their complex-valued counterparts.

As described in Section S8 of the supplemental material, the  $5 \times 4$  binning case performed extremely well using a straightforward sequential CNN architecture. After training, we were able to accurately realize 100% of the target responses over both the training and validation sets. Unfortunately, the purely sequential architecture of the network did not work as well for the  $3 \times 3$  binning configuration (as discussed in Section S10 of the supplemental material). The increased complexity implies that we need a more complex network, so we turned to approaches successfully used in modern image classification, specifically inception modules [55, 56].

An inception module is designed to promote sparse feature representation using available dense components [55] and works by optimizing the receptive field coverage of a convolutional network. The receptive field is the num-

ber of points in input space that contribute to a point at a given layer of the deep learning network and is described in detail in Section S9 of the supplemental material. Through the use of parallelization and concatenation, the receptive field sizes at a layer are conserved for subsequent layers to utilize, extracting features through the width of the deep learning network as well as its depth.

The original inception module was developed for image processing and operates in a true 2D space, with full 2D convolutions. It uses 4 parallel paths with CNN layers containing unit length kernels for buffering and conditioning, along with 3 and 5 sample length kernels for feature extraction, and a max pool layer to improve performance [55]. There have been several variations of the inception module; however, none operate in the pseudo-2D space we desire. For our “images”, the frequency spacing along columns is the resolution of the network analyzer (31.25 kHz), while the frequency spacing along rows is the separation between local windows (10 MHz). The difference in sampling means we need to treat the rows and columns accordingly and avoid traditional 2D convolutions that assume uniform sampling. Therefore, we modified the general architecture of the inception module to perform 1D convolutions over the 10 MHz local frequency windows. The 1D convolutional filters then extract local features over the 10 MHz windows, while the relationship between the filters acts as a dense or fully connected layer, extracting global features over the full 1 GHz measurement window.

From previous work with the cavity, we found that the mean mode spacing is  $\sim 125$  kHz and we demonstrated the ability to generate strong nulls over a 500 kHz bandwidth [18]. This suggests we should use a pooling window of 125 kHz and allow the receptive field to increase by 125 kHz and 500 kHz at each stage, or layer in the deep learning network. After experimenting, we found that adding a 5th stage which increased the receptive field by 1 MHz helped to further improve performance. The final version, which we refer to as a “Terrapin module”, is shown schematically in Fig. 4, and provides the fourth and final major novel technical contribution of our approach.

With a deep learning network containing 4 Terrapin modules in series, we were able to get excellent performance for the  $5 \times 4$  and  $3 \times 3$  binning configurations with only 4,000 sets of training data. As discussed in Section S11 of the supplemental material, the  $2 \times 2$  configuration required 10,000 sets of data for a similar level of performance. The smaller effective elements in this configuration produce responses with a larger degree of correlation. Thus, more data is required for the network to learn and distinguish the more subtle relationships between metasurface command configurations and scattering matrix responses,  $S_{21}(f)$ .

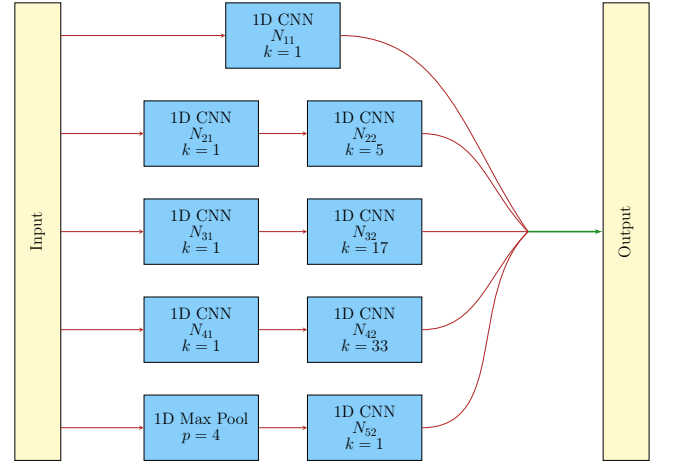


Figure 4. **Terrapin Module Architecture.** Five parallel branches with 8 1D convolutional neural network (CNN) layers and a max pool layer are used in the module. The module operates on the pseudo-2D data format discussed previously, and the input layer can ingest either the raw measured  $S_{21}$  parameters or the outputs from a previous Terrapin module. The output layer is then connected either to a subsequent Terrapin module for additional processing or to the final output layer for conversion to metasurface commands. Each CNN includes a 1D convolution, a batch normalization, and a rectified linear unit activation function. The 2nd level CNNs have kernel lengths of 5, 17, and 33 to increase the receptive field by 125 kHz, 500 kHz, and 1 MHz, respectively. A 1D max pooling layer with pool size of 4 is included to provide a pooling window of 125 kHz as well. The quantity  $N_{xx}$  indicates a tunable parameter for the number of convolutional filters at each branch and stage, acting as a dense or fully connected layer for the global correlations. The convolutions with unit length kernels serve to buffer and condition the inputs to each stage, and the single layer 1st branch maintains the receptive field sizes from previous modules. The outputs of each branch are concatenated together to form the module output, preserving the receptive field sizes for subsequent layers.

## V. RESULTS

The primary objective of this work is to demonstrate that deep wavefront shaping is a viable technique for intentionally scrambling (or unscrambling) waves propagating through a complex scattering environment, enabling intelligent wavefront shaping in a chaotic cavity. In this section, we shown how our deep wavefront shaping approach accurately determines metasurface commands from measured cavity scattering parameters.

Training results for the  $5 \times 4$  and  $3 \times 3$  binning configurations are provided in Sections S8 and S10 of the supplemental material, while training results for the  $2 \times 2$  binning configuration are shown in Fig. 5. The training data consists of 10,000 random realizations of metasurface commands, representing an extremely small fraction of the  $1.8 \times 10^{72}$  possible configurations. The data was split into 7500 sets for training and 2500 sets for valida-

tion to ensure the validation process is unbiased. The evolution of the loss function is shown in Fig. 5 (a) and the evolution of the accuracy is shown in Fig. 5 (b). The loss function was chosen as the mean absolute error, or the  $\mathcal{L}_1$  norm, between determined and actual metasurface commands. Accuracy is the fraction of sets that was determined without error and provides a more conservative estimate of performance. The variation around Epoch 45 is due to choosing an aggressive initial learning rate and the impact of reducing the learning rate on a plateau can be seen at Epoch 55. These panels demonstrate that we were able to obtain high accuracy and a small loss function for both the training and validation data sets.

The trained model did not have perfect accuracy but was able to determine 2,443 out of 2,500 sets in the validation data without error for an accuracy of 97.7%. One set had 2 errors and 56 sets had a single error, as shown in Fig. 5 (c). A comparison of the determined and true commands is shown in Fig. 5 (d)-(g). These panels show that for the worst case set with two errors, the network was not highly confident in the results as the determined command probabilities were 0.41 and 0.73. Finally, the deep learning network architecture is shown in Fig. 5 (h), which contains 4 Terrapin modules separated by max pooling layers. The output stage consists of a global average pooling layer that converts complex values to magnitude and a dense layer to provide the appropriate number of outputs. A sigmoid activation function is used at the output to limit the determined commands to real numbers between 0 and 1.

To further test the trained deep learning network, we adopted the on-line, closed loop configuration as shown in Fig. 6 (a). Commands were applied to the metasurface and the  $S_{21}$  response was measured and then passed through the trained deep learning model to verify accuracy. When the deep learning determined commands had errors, the determined commands were applied to the metasurface so that the difference in  $S_{21}$  responses could be computed. We define the difference,  $\Delta S_{21}$ , between two measured  $S_{21}$  responses,  $S_{21}^a$  and  $S_{21}^b$  through the  $\mathcal{L}_2$  (Euclidean) norm,  $\|S_{21}(f)\|_2 = \sqrt{\sum_f |S_{21}(f)|^2}$ . The summation is taken over the full measured frequency range (3-4 GHz) and  $\Delta S_{21}$  is defined as

$$\Delta S_{21} = 2 \frac{\|S_{21}^a(f) - S_{21}^b(f)\|_2}{\|S_{21}^0(f)\|_2 + \|S_{21}^1(f)\|_2} \quad (1)$$

The normalization factor here is determined by the average of the  $\mathcal{L}_2$  norms of the active commands (all 1s),  $S_{21}^1$ , and the inactive commands (all 0s),  $S_{21}^0$ . To understand how  $\Delta S_{21}$  depends on the difference between commands, we first identified the minimum Hamming distance for each of the 10,000 sets in the training data. The Hamming distance is simply the number of elements that are different between 2 sets of commands. It is a useful metric for comparing command sets, but does not

include scaling or correlation based on position; in some cases, the impact of toggling an element in the center may be significantly different than the impact of toggling an element on the edge of the metasurface.

The smallest Hamming distance between the training data sets ranged from a single element to 19 elements (out of 60). A series of whisker box plots showing  $\Delta S_{21}$  for the various Hamming distances is shown in Fig. 6 (b). The general trend shows an increase in  $\Delta S_{21}$  with an increase in the Hamming distance. While the relationship is nonlinear, the dynamic range in  $\Delta S_{21}$  for Hamming distances up to 1/3 of the total number of elements is large, approximately an order of magnitude.

Validation of the deep learning network in the configuration shown in Fig. 6 (a) was performed periodically after collecting the training data and the results are shown in Fig. 6 (c) at 2 hours, (d) at 36 hours (1.5 days), and (e) at 72 hours (3 days). Over time the scattering environment is expected to “age” and systematic changes to the scattering environment will occur. The blue diamonds show cases where there was a single error, and the black dots show cases where there were 2 errors. Each on-line validation experiment showed  $\sim 95\%$  accuracy and the resulting  $\Delta S_{21}$  for errors was small compared to the observed statistical extent of  $\Delta S_{21}$  for single element Hamming distances. This suggests that even when the deep learning network is unable to determine the commands completely accurately, the resulting difference in  $S_{21}$  is very small. As shown in Section S12 of the supplemental material, the accuracy was still  $>85\%$  after 120 hours (5 days), but dropped to  $\sim 65\%$  after 9 days.

The number of errors and number of cases with more than one error increases with time, showing the “aging” effect of the cavity, which can be quantified through the concept of scattering fidelity. Scattering fidelity is the normalized correlation as a function of time between two cavity responses with the same initial conditions [57]. Because a chaotic cavity is sensitive to small changes in the boundary conditions, such as volume perturbations, the scattering fidelity will decay over time [44–46]. Loss in scattering fidelity means that the accuracy of any trained deep learning network has a finite lifetime, so we must periodically retrain the network on new training data to maintain accuracy. In our case, we have demonstrated that the deep learning network can determine metasurface commands with high accuracy ( $> 95\%$ ) for at least 72 hours (3 days) after the initial training data collection, and with reasonable accuracy ( $> 85\%$ ) up to 120 hours (5 days) after the initial training data collection. Large variations in environmental conditions, such as temperature or humidity, will introduce larger perturbations and more rapidly degrade the scattering fidelity.

## VI. SUMMARY AND DISCUSSION

In this paper, we demonstrated the use of a deep learning network to enable intelligent wavefront shap-



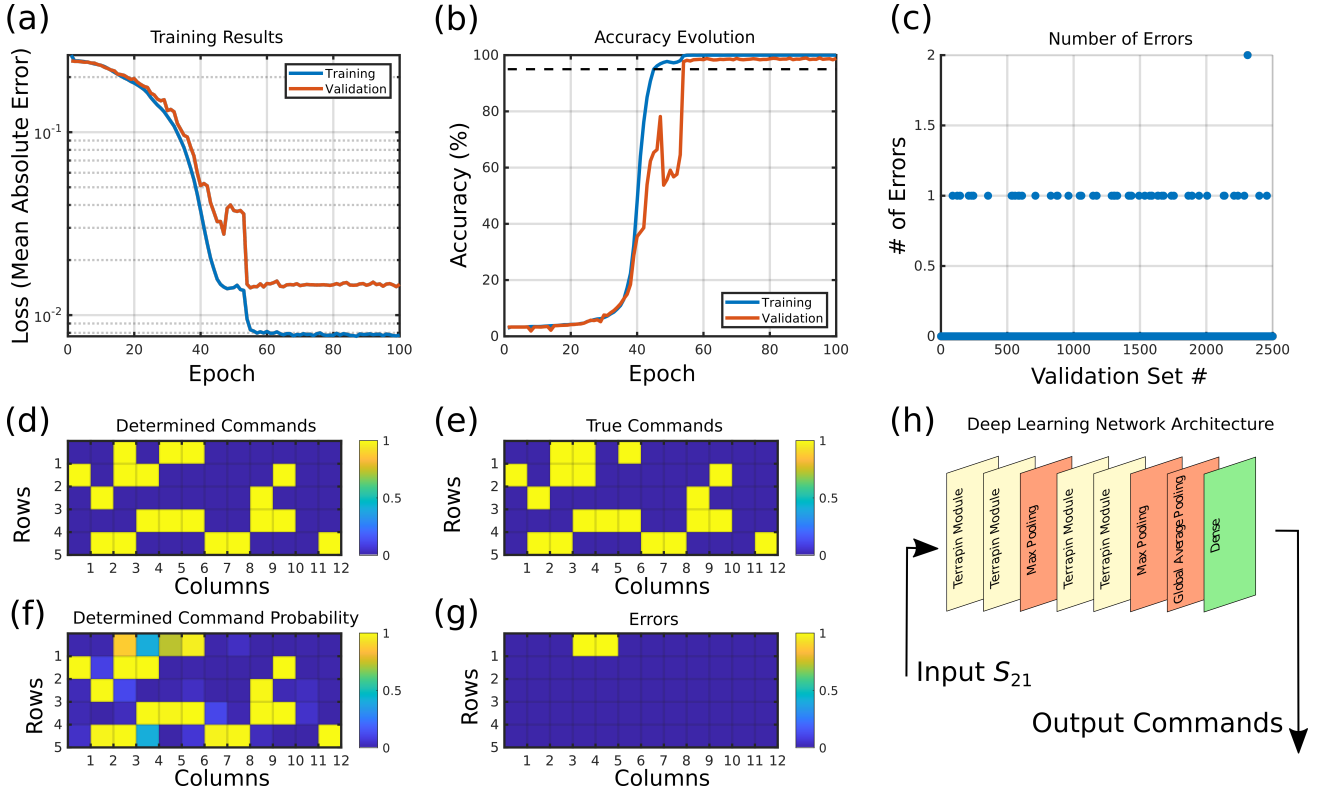


Figure 5. **Deep learning performance with complex-valued layers for 2x2 binning.** (a) Evolution of the loss function for the training and validation sets over 100 epochs. The learning rate is reduced at Epoch 55, inducing an additional reduction in the loss function. The initial learning rate was aggressive, resulting in a large variation in the validation loss function between Epochs 45-50. (b) Evolution of the accuracy for the training and validation sets over 100 epochs, the dashed black line identifies 95% accuracy. (c) Number of errors over the validation set for the trained model, showing a total of 58 errors and 97.7% accuracy. The maximum number of errors in a single set was 2 (out of 60 elements), which occurred once. (d) Determined commands for validation set #2311 showing the output from the deep learning network. (e) True commands for validation set #2311 showing what was actually applied to the metasurface. (f) Determined command probability for validation set #2311, showing the raw outputs from the deep learning network prior to rounding. This panel shows that the 2 elements determined incorrectly have command probabilities of 0.41 and 0.73, meaning the network was not highly confident in the result. (g) Errors, or incorrectly determined commands for validation set #2311, showing the 2 elements that were determined incorrectly. (h) Schematic architecture for the deep learning network showing 4 Terrapin modules interspersed with max pooling layers. The output section consists of a global average pooling layer and a dense layer with a sigmoid activation function.

ing in complex environments. Major novel aspects include complex-valued deep learning layers that exploit both phase and amplitude information, binning of the metasurface elements, a pseudo-2D data format that allows features to be extracted over both narrow and wide bandwidths, and a Terrapin module that enhances the receptive field, providing width and depth to the network.

One of the primary limitations of traditional deep learning is the amount of data required to train the networks. This is especially concerning in light of the fact that loss of scattering fidelity requires periodically collecting new training data. We have demonstrated the ability to train highly accurate networks with a limited amount of training data, requiring far fewer sets than the number of possible combinations of commands. We have also demonstrated that the accuracy can be maintained for a period of at least several days. This indicates

that successful training on a reduced amount of data is possible, provided it is sufficiently diverse. Diversity in both the metasurface commands and the measured responses is then a key aspect in setting up any potential autonomous system.

For on-the-fly learning and adaptation to changing environmental conditions, we propose the future use of reinforcement learning [58, 59], which is at the intersection of artificial intelligence and optimal control. Reinforcement learning uses an agent that interacts with an environment to learn about it and then manipulate that environment in order to maximize (minimize) a reward (cost function), leading to the development of optimal control policies. In particular, the subset of reinforcement learning known as deep or double deep “Q” learning is gaining traction as a method for controlling quantum states [60–62]. Deep “Q” learning uses a deep learning network to

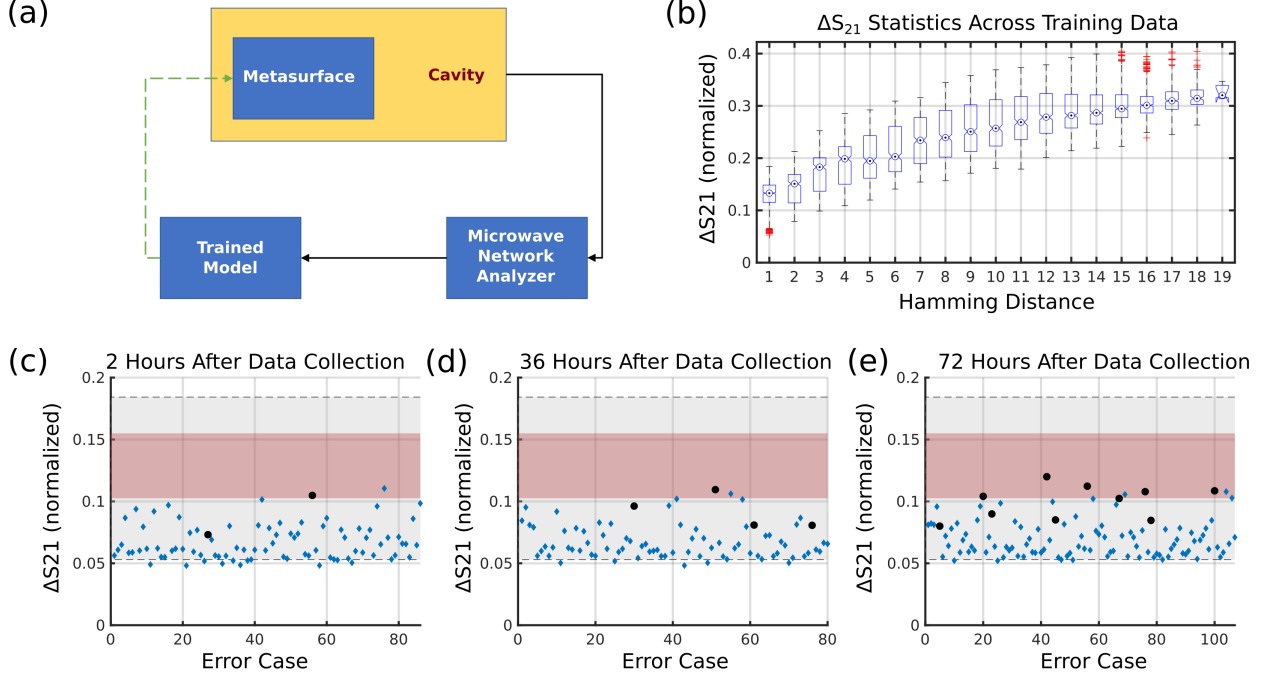


Figure 6. **On-line performance verification.** (a) Closed loop validation configuration. Commands were applied to the metasurface inside the cavity, the corresponding  $S_{21}$  response was measured on the PNA, and the results were passed through the trained deep learning network. Errors for the trained model were then measured to determine the difference in  $S_{21}$ ,  $\Delta S_{21}$ , between the two command sets. (b)  $\Delta S_{21}$  statistics for the minimum Hamming distance across the 10,000 sets from the training data. Whisker plots are given for the smallest Hamming distance for each case, and show the mean value, 25<sup>th</sup> and 75<sup>th</sup> percentiles, and maximum and minimum values. (c) through (e)  $\Delta S_{21}$  for online validation sets taken a specified time after the training data was collected. The shaded regions show the extent of the single element Hamming distance whisker box plot from panel (b). The grey region shows the full range from maximum to minimum, and the red region shows the 25<sup>th</sup> and 75<sup>th</sup> percentiles. The blue diamonds indicate cases with a single error, while the black circles indicate cases with 2 errors. These panels show that the  $\Delta S_{21}$  for errors is very small, and in the lower region of the statistics covered by observed cases with single element Hamming distances. (c) Validation 2 hours after collecting training data, 2000 sets of commands were tested with 86 errors for an accuracy of 95.7%. (d) Validation 36 hours after collecting training data, 2000 sets of commands were tested with 80 errors for an accuracy of 96%. (e) Validation 72 hours after collecting training data, 2000 sets of commands were tested with 107 errors for an accuracy of 94.7%.

estimate a quality matrix that scores the result of taking a particular action, while double deep “Q” learning uses two estimates to limit the implementation of poor control policies from overestimation [63]. The deep learning network architecture developed in this paper is well suited for estimation of this quality matrix.

Specification of an arbitrary scattering condition in the current implementation is cumbersome, as the complete  $S_{21}$  response over the full 3-4 GHz measurement window must be defined. For practical engineering applications, we prefer a simpler method of defining a desired wave scattering condition. Deep reinforcement learning also helps in this case, as it scores the performance of an agent through a scalar, positive, and real-valued metric. The agent uses the deep learning network to learn the relationship between metasurface commands and  $S_{21}$  responses, but the complicated details are hidden from the user. There are therefore 2 learning components to deep

reinforcement learning: an inner deep learning network that learns how to map  $S_{21}$  responses onto metasurface commands, and an outer agent based loop that learns how to use the inner deep learning network to optimize the desired metric. This metric can be the total power in a specified bandwidth for cold spot generation, the magnitude of the eigenvalues of the full  $S$ -matrix at a given frequency for coherent perfect absorption, or the bit error rate for communications systems.

Learning from scratch can be slow and may not be fast enough to adapt to changing environmental conditions. In this case, transfer learning, or using information about a similar problem to accelerate training for another one, can be incorporated into the reinforcement learning strategy [64].

Several concerns must be addressed to enable practical fielded hardware systems. First, the sensing component must be reduced in cost and size. The availability of

software defined radio (SDR) architectures presents an ideal path here, with many inexpensive platforms readily available. Compact devices such as the bladeRF [65] can replace the bulky network analyzer. SDRs have limited instantaneous bandwidth, typically 10-20 MHz, so modifications would be required to the pseudo-2D data representation. Second, processing large deep learning models on power hungry GPUs may exceed the allowable footprint in terms of both cost and power consumption. Deep learning models can be compressed by pruning and quantization [66], and the explosion of edge intelligence for connected devices in the Internet of Things is leading to more efficient embedded deep learning systems. An example is the Jetson series of embedded GPUs from NVIDIA; the currently available TX2 series can provide up to 1.26 trillion floating point operations per second on a 256-core GPU while consuming only 10-20 W of power [67].

In closing, we have shown that deep wavefront shaping provides an important step towards realizing intelligent reconfigurable metasurfaces for smart radio envi-

ronments. Potential applications in the domain of electromagnetics include wireless power transfer, protection of sensitive electronic components, optimization of wireless networks, micromanipulation of objects, and nonlinear time reversal. Our technique is applicable to general wave chaotic scattering systems and is not strictly limited to electromagnetic waves. Adopting deep wavefront shaping to control the system scattering response with metasurfaces that interact with seismic waves [20, 21] or quantum waves [22] will unlock many innovative applications for wave chaotic systems.

## VII. ACKNOWLEDGEMENTS

We thank Zerotti Woods of JHU/APL for supporting many fruitful discussions on applied deep learning. Funding for this work was provided through AFOSR COE Grant FA9550-15-1-0171 and ONR Grant N000141912481.

- 
- [1] Z. B. Drikas, J. Gil Gil, S. K. Hong, T. D. Andreadis, J.-H. Yeh, B. T. Taddese, and S. M. Anlage, Application of the Random Coupling Model to Electromagnetic Statistics in Complex Enclosures, *IEEE Transactions on Electromagnetic Compatibility* **56**, 1480 (2014).
  - [2] M. D. Renzo, M. Debbah, D.-T. Phan-Huy, A. Zappone, M.-S. Alouini, C. Yuen, V. Sciancalepore, G. C. Alexandropoulos, J. Hoydis, H. Gacanin, J. de Rosny, A. Bounceur, G. Lerosey, and M. Fink, Smart radio environments empowered by reconfigurable ai meta-surfaces: an idea whose time has come, *EURASIP Journal on Wireless Communications and Networking* **129**, 2450 (2019).
  - [3] M. Di Renzo, A. Zappone, M. Debbah, M. S. Alouini, C. Yuen, J. de Rosny, and S. Tretjakov, Smart radio environments empowered by reconfigurable intelligent surfaces: How it works, state of research, and the road ahead, *IEEE Journal on Selected Areas in Communications* **38**, 2450 (2020).
  - [4] M. Horodyski, M. Kühmayer, A. Brandstötter, K. Pichler, Y. V. Fyodorov, U. Kuhl, and S. Rotter, Optimal wave fields for micromanipulation in complex scattering environments, *Nature Photonics* **14**, 149 (2020).
  - [5] M. Frazier, B. Taddese, T. Antonsen, and S. M. Anlage, Nonlinear Time Reversal in a Wave Chaotic System, *Physical Review Letters* **110**, 063902 (2013).
  - [6] B. Xiao, T. M. Antonsen, E. Ott, and S. M. Anlage, Focusing waves at arbitrary locations in a ray-chaotic enclosure using time-reversed synthetic sonas, *Physical Review E* **93**, 052205 (2016).
  - [7] I. M. Vellekoop and A. P. Mosk, Focusing coherent light through opaque strongly scattering media, *Optics Letters* **32**, 2309 (2007).
  - [8] A. Mosk, A. Lagendijk, G. Lerosey, and M. Fink, Controlling waves in space and time for imaging and focusing in complex media, *Nature Photonics* **6**, 283 (2012).
  - [9] M. Booth, D. Andrade, D. Burke, B. Patton, and M. Zurauskas, Aberrations and adaptive optics in super-resolution microscopy, *Microscopy* **64**, 251 (2015).
  - [10] M. Collini, F. Radaelli, L. Sironi, N. G. Ceffa, L. D'Alfonso, M. Bouzin, and G. Chirico, Adaptive optics microspectrometer for cross-correlation measurement of microfluidic flows, *Journal of Biomedical Optics* **24**, 1 (2019).
  - [11] M. Dupré, P. del Hougne, M. Fink, F. Lemoult, and G. Lerosey, Wave-Field Shaping in Cavities: Waves Trapped in a Box with Controllable Boundaries, *Physical Review Letters* **115**, 017701 (2015).
  - [12] N. Kaina, M. Dupré, G. Lerosey, and M. Fink, Shaping complex microwave fields in reverberating media with binary tunable metasurfaces, *Scientific Reports* **4**, 6693 (2015).
  - [13] P. del Hougne, F. Lemoult, M. Fink, and G. Lerosey, Spatiotemporal Wave Front Shaping in a Microwave Cavity, *Physical Review Letters* **117**, 134302 (2016).
  - [14] P. del Hougne, M. Davy, and U. Kuhl, Optimal Multiplexing of Spatially Encoded Information across Custom-Tailored Configurations of a Metasurface-Tunable Chaotic Cavity, *Physical Review Applied* **13**, 041004 (2020).
  - [15] J.-B. Gros, P. del Hougne, and G. Lerosey, Tuning a regular cavity to wave chaos with metasurface-reconfigurable walls, *Physical Review A* **101**, 061801 (2020).
  - [16] M. F. Imani, D. R. Smith, and P. del Hougne, Perfect absorption in a disordered medium with programmable meta-atom inclusions, *Advanced Functional Materials* **30**, 2005310 (2020).
  - [17] P. del Hougne, D. V. Savin, O. Legrand, and U. Kuhl, Implementing nonuniversal features with a random matrix theory approach: Application to space-to-configuration multiplexing, *Phys. Rev. E* **102**, 010201 (2020).

- [18] B. W. Frazier, T. M. Antonsen, S. M. Anlage, and E. Ott, Wavefront shaping with a tunable metasurface: Creating cold spots and coherent perfect absorption at arbitrary frequencies, *Phys. Rev. Research* **2**, 043422 (2020).
- [19] P. del Hougne, B. Yeo, P. Besnier, and M. Davy, On-demand coherent perfect absorption in complex scattering systems: time delay divergence and enhanced sensitivity to perturbations, [arXiv:2010.06438 \[physics.class-ph\]](#) (2020).
- [20] A. Palermo and A. Marzani, Control of Love waves by resonant metasurfaces, *Scientific Reports* **8**, 7234 (2018).
- [21] Y. He, T. Chen, and X. Song, Manipulation of seismic rayleigh waves using a phase-gradient rubber metasurface, *International Journal of Modern Physics B* **34**, 2050142 (2020).
- [22] R. Bekenstein, I. Pikovski, H. Pichler, E. Shahmoon, S. F. Yelin, and M. D. Lukin, Quantum metasurfaces with atom arrays, *Nature Physics* **16**, 676 (2020).
- [23] I. Vellekoop and A. Mosk, Phase control algorithms for focusing light through turbid media, *Optics Communications* **281**, 3071 (2008).
- [24] C. Dorrer and J. Qiao, Direct binary search for improved coherent beam shaping and optical differentiation wavefront sensing, *Applied Optics* **57**, 8557 (2018).
- [25] S. Ma, B. Xiao, R. Hong, B. Addissie, Z. Drikas, T. Antonsen, E. Ott, and S. Anlage, Classification and Prediction of Wave Chaotic Systems with Machine Learning Techniques, *Acta Physica Polonica A* **136**, 757 (2019).
- [26] D. Liu, Y. Tan, E. Khoram, and Z. Yu, Training Deep Neural Networks for the Inverse Design of Nanophotonic Structures, *ACS Photonics* **5**, 1365 (2018).
- [27] C. C. Nadell, B. Huang, J. M. Malof, and W. J. Padilla, Deep learning for accelerated all-dielectric metasurface design, *Optics Express* **27**, 27523 (2019).
- [28] S. An, C. Fowler, B. Zheng, M. Y. Shalaginov, H. Tang, H. Li, L. Zhou, J. Ding, A. M. Agarwal, C. Rivero-Baleine, K. A. Richardson, T. Gu, J. Hu, and H. Zhang, A Deep Learning Approach for Objective-Driven All-Dielectric Metasurface Design, *ACS Photonics* **6**, 3196 (2019).
- [29] T. Qiu, X. Shi, J. Wang, Y. Li, S. Qu, Q. Cheng, T. Cui, and S. Sui, Deep Learning: A Rapid and Efficient Route to Automatic Metasurface Design, *Advanced Science* **6**, 1900128 (2019).
- [30] I. Sajedian, H. Lee, and J. Rho, Double-deep Q-learning to increase the efficiency of metasurface holograms, *Scientific Reports* **9**, 10899 (2019).
- [31] C. Yeung, J.-M. Tsai, B. King, Y. Kawagoe, D. Ho, M. W. Knight, and A. P. Raman, Elucidating the Behavior of Nanophotonic Structures through Explainable Machine Learning Algorithms, *ACS Photonics* **7**, 2309 (2020).
- [32] P. R. Wiecha and O. L. Muskens, Deep Learning Meets Nanophotonics: A Generalized Accurate Predictor for Near Fields and Far Fields of Arbitrary 3D Nanostructures, *Nano Letters* **20**, 329 (2020).
- [33] J. Jiang, M. Chen, and J. A. Fan, Deep neural networks for the evaluation and design of photonic devices, *Nature Reviews Materials* (2020).
- [34] R. Unni, K. Yao, and Y. Zheng, Deep Convolutional Mixture Density Network for Inverse Design of Layered Photonic Structures, *ACS Photonics* **7**, 2703 (2020).
- [35] A. Mall, A. Patil, A. Sethi, and A. Kumar, A cyclical deep learning based framework for simultaneous inverse and forward design of nanophotonic metasurfaces, *Scientific Reports* **10**, 19427 (2020).
- [36] S. An, B. Zheng, M. Y. Shalaginov, H. Tang, H. Li, L. Zhou, J. Ding, A. M. Agarwal, C. Rivero-Baleine, M. Kang, K. A. Richardson, T. Gu, J. Hu, C. Fowler, and H. Zhang, Deep learning modeling approach for metasurfaces with high degrees of freedom, *Optics Express* **28**, 31932 (2020).
- [37] L. Li, Y. Shuang, Q. Ma, H. Li, H. Zhao, M. Wei, C. Liu, C. Hao, C.-W. Qiu, and T. J. Cui, Intelligent metasurface imager and recognizer, *Light: Science & Applications* **8**, 97 (2019).
- [38] L. Li, H. Ruan, C. Liu, Y. Li, Y. Shuang, A. Alù, C.-W. Qiu, and T. J. Cui, Machine-learning reprogrammable metasurface imager, *Nature Communications* **10**, 1082 (2019).
- [39] P. del Hougne, M. F. Imani, A. V. Diebold, R. Horstmeyer, and D. R. Smith, Learned Integrated Sensing Pipeline: Reconfigurable Metasurface Transceivers as Trainable Physical Layer in an Artificial Neural Network, *Advanced Science* **7**, 1901913 (2020).
- [40] P. del Hougne, Robust position sensing with wave fingerprints in dynamic complex propagation environments, *Phys. Rev. Research* **2**, 043224 (2020).
- [41] M. del Hougne, S. Gigan, and P. del Hougne, Deeply Sub-Wavelength Localization with Reverberation-CodedAperture, [arXiv:2102.05642 \[physics.app-ph\]](#) (2021).
- [42] C. Qian, B. Zheng, Y. Shen, L. Jing, E. Li, L. Shen, and H. Chen, Deep-learning-enabled self-adaptive microwave cloak without human intervention, *Nature Photonics* **14**, 383 (2020).
- [43] T. Shan, X. Pan, M. Li, S. Xu, and F. Yang, Coding Programmable Metasurfaces Based on Deep Learning Techniques, *IEEE Journal on Emerging and Selected Topics in Circuits and Systems* **10**, 114 (2020).
- [44] R. Schäfer, H.-J. Stöckmann, T. Gorin, and T. H. Seligman, Experimental verification of fidelity decay: From perturbative to fermi golden rule regime, *Phys. Rev. Lett.* **95**, 184102 (2005).
- [45] B. T. Taddese, J. Hart, T. M. Antonsen, E. Ott, and S. M. Anlage, Sensor based on extending the concept of fidelity to classical waves, *Applied Physics Letters* **95**, 114103 (2009).
- [46] B. T. Taddese, T. M. Antonsen, E. Ott, and S. M. Anlage, Sensing small changes in a wave chaotic scattering system, *Journal of Applied Physics* **108**, 114911 (2010).
- [47] R. L. Schmid, D. B. Shrekenhamer, O. F. Somerlock, A. C. Malone, T. A. Sleasman, and R. S. Awadallah, S-band GaAs FET Reconfigurable Reflectarray for Passive Communications, in *2020 IEEE Radio and Wireless Symposium (RWS)* (IEEE, San Antonio, TX, USA, 2020) pp. 91–93.
- [48] Y. Deng, S. Ren, K. Fan, J. M. Malof, and W. J. Padilla, Neural-adjoint method for the inverse design of all-dielectric metasurfaces, *Opt. Express* **29**, 7526 (2021).
- [49] J. A. Hart, T. M. Antonsen, and E. Ott, Effect of short ray trajectories on the scattering statistics of wave chaotic systems, *Physical Review E* **80**, 041109 (2009).
- [50] J.-H. Yeh, J. A. Hart, E. Bradshaw, T. M. Antonsen, E. Ott, and S. M. Anlage, Experimental examination of the effect of short ray trajectories in two-port wave-chaotic scattering systems, *Physical Review E* **82**, 041114 (2010).



- [51] C. Trabelsi, O. Bilaniuk, Y. Zhang, D. Serdyuk, S. Subramanian, J. F. Santos, S. Mehri, N. Rostamzadeh, Y. Bengio, and C. J. Pal, Deep Complex Networks, arXiv:1705.09792 [cs] (2018), [arXiv:1705.09792 \[cs\]](#).
- [52] O. Moran, P. Caramazza, D. Faccio, and R. Murray-Smith, Deep, complex, invertible networks for inversion of transmission effects in multimode optical fibres, in *Advances in Neural Information Processing Systems*, Vol. 31, edited by S. Bengio, H. Wallach, H. Larochelle, K. Grauman, N. Cesa-Bianchi, and R. Garnett (Curran Associates, Inc., 2018) pp. 3280–3291.
- [53] P. Caramazza, O. Moran, R. Murray-Smith, and D. Faccio, Transmission of natural scene images through a multimode fibre, *Nature Communications* **10**, 2029 (2019).
- [54] S. Popoff, [complexpytorch](#), <https://github.com/wavefrontshaping/complexPyTorch> (2019).
- [55] C. Szegedy, Wei Liu, Yangqing Jia, P. Sermanet, S. Reed, D. Anguelov, D. Erhan, V. Vanhoucke, and A. Rabinovich, Going deeper with convolutions, in *2015 IEEE Conference on Computer Vision and Pattern Recognition (CVPR)* (IEEE, Boston, MA, USA, 2015) pp. 1–9.
- [56] C. Szegedy, V. Vanhoucke, S. Ioffe, J. Shlens, and Z. Wojna, Rethinking the Inception Architecture for Computer Vision, in *2016 IEEE Conference on Computer Vision and Pattern Recognition (CVPR)* (IEEE, Las Vegas, NV, USA, 2016) pp. 2818–2826.
- [57] B. T. Taddese, G. Gradoni, F. Moglie, T. M. Antonsen, E. Ott, and S. M. Anlage, Quantifying volume changing perturbations in a wave chaotic system, *New Journal of Physics* **15**, 023025 (2013).
- [58] C. J. C. H. Watkins, *Learning from Delayed Rewards*, Ph.D., King’s College (1989).
- [59] D. P. Bertsekas, *Reinforcement learning and optimal control* (Athena Scientific, 2019).
- [60] M. Bukov, A. G. Day, D. Sels, P. Weinberg, A. Polkovnikov, and P. Mehta, Reinforcement Learning in Different Phases of Quantum Control, *Physical Review X* **8**, 031086 (2018).
- [61] J. Mackeprang, D. B. R. Dasari, and J. Wrachtrup, A reinforcement learning approach for quantum state engineering, *Quantum Machine Intelligence* **2**, 5 (2020).
- [62] M. M. Wauters, E. Panizon, G. B. Mbeng, and G. E. Santoro, Reinforcement-learning-assisted quantum optimization, *Physical Review Research* **2**, 033446 (2020).
- [63] H. van Hasselt, A. Guez, and D. Silver, Deep Reinforcement Learning with Double Q-learning, [arXiv:1509.06461 \[cs\]](#) (2015).
- [64] M. E. Taylor and P. Stone, Transfer Learning for Reinforcement Learning Domains: A Survey, *Journal of Machine Learning Research* **10**, 1633 (2009).
- [65] Nuand, [bladeRF](#), <https://www.nuand.com>.
- [66] S. Han, H. Mao, and W. J. Dally, Deep Compression: Compressing Deep Neural Networks with Pruning, Trained Quantization and Huffman Coding, arXiv:1510.00149 [cs] (2016), [arXiv:1510.00149 \[cs\]](#).
- [67] NVIDIA, *Jetson Embedded Systems*, <https://www.nvidia.com/en-us/autonomous-machines/embedded-systems/>.

# Supplemental Material for Deep Wavefront Shaping: Intelligent Control of Complex Scattering Responses with a Programmable Metasurface

Benjamin W. Frazier,<sup>1,2,3,\*</sup> Thomas M. Antonsen, Jr.,<sup>1,2,4</sup> Steven M. Anlage,<sup>2,4,5</sup> and Edward Ott<sup>1,2,4</sup>

<sup>1</sup>*Institute for Research in Electronics and Applied Physics,  
University of Maryland, College Park, MD 20742, USA*

<sup>2</sup>*Department of Electrical and Computer Engineering,  
University of Maryland, College Park, MD 20742, USA*

<sup>3</sup>*Johns Hopkins University Applied Physics Laboratory, Laurel, MD 20723, USA*

<sup>4</sup>*Department of Physics, University of Maryland, College Park, MD 20742, USA*

<sup>5</sup>*Quantum Materials Center, University of Maryland, College Park, MD 20742, USA*

(Dated: March 1, 2025)

## S1. CAVITY AND EXPERIMENTAL CONFIGURATION

The cavity used has a volume of  $\sim 0.76 \text{ m}^3$  and includes 3 ports, with ports 1 and 3 used to inject signals and port 2 used for scoring. The cavity configuration and experimental schematic are shown in Fig. S1. Each port is connected to an ultra wideband antenna (UWB) and the nominal measurement window is 3-4 GHz. A line-of-sight block is used to obstruct the direct transmission path from port 2 to both ports 1 and 3, and an Arduino controlled mechanical mode stirrer is included to allow collection of an ensemble of cavity realizations. The experimental setup is controlled by a MacBook Pro laptop, with an Agilent N5242A network analyzer used to measure cavity  $S$ -parameters. Ports 1 and 3 can be driven either independently or collectively with a relative phase shift provided by a NARDA phase shifter. To reduce the cavity symmetry, irregular scattering objects were installed on the walls.

In the frequency range of interest, 3-4 GHz, the Weyl formula [S1] predicts approximately 8524 resonant modes of the complex enclosure and the measured quality factor of the cavity is roughly  $5.5 \times 10^3$  [S2]. A resonance mode width is then  $\sim 5$  times greater than the mean mode spacing, which means there is some local overlap between modes.

## S2. INVERSE PROBLEM DEFINITION

With complex geometries, multiple reflections create intricate interference patterns at the antennas, producing chaotic fluctuations [S3, S4]. This leads to a complicated relationship between metasurface commands and cavity scattering parameters. For a metasurface that is small relative to the cavity, the effective strength of the metasurface commands on the cavity scattering parameters is reduced. This results in high correlation between measurements taken with different sets of commands and creates problems for uniqueness, as many potential solutions

are extremely similar. In addition, the scattering process is linear, but the relationship between metasurface commands and measured scattering parameters is not necessarily so, particularly for measurements in the temporal domain. Transmission matrix based approaches [S5, S6] are useful for characterizing the cavity, but are not feasible for generating control policies under this configuration.

Mathematically, the metasurface commands can be found from an inverse problem of the form  $\mathbf{x} = \mathbf{H}^{-1}\mathbf{m}$ , where  $\mathbf{H}$  is a transfer function operator,  $\mathbf{x}$  is a vector of metasurface commands, and  $\mathbf{m}$  is a vector of measurements. Unfortunately, the inverse problem is not well posed, so measuring  $\mathbf{H}$ , let alone inverting it, is not trivial.

## S3. DEEP LEARNING AND NEURAL NETWORK LAYERS

The concept of depth in deep learning comes from complexity theory as defined for circuits, with depth being the longest path from an input to an output [S7]. The number of potential paths or ways to reuse features grows exponentially with depth, which leads to progressively more abstract features [S8, S9]. Depth is therefore an important characteristic of a network to leverage as it enhances the expressive power of the network and allows it to learn a rich, hierarchical feature representation [S10, S11]. In physics, deep learning has repeatedly been shown to be unreasonably effective for extremely complicated problems [S12].

A deep network is divided into layers, with the interior layers often referred to as hidden, as they are unobservable from the input or the output. Networks come in many different shapes and sizes; no single type is optimal for all problems, a consequence of the “No Free Lunch” theorem [S13]. The networks described in this paper utilize 4 different types of layers: 1) Dense, linear, or fully connected layers characterized by the number of neurons. The output is a linear combination of the inputs; 2) Convolutional layers characterized by the number of filters and the length of the kernel. The output is the result of convolving the inputs with the kernels; 3)

\* Benjamin.Frazier@jhuapl.edu

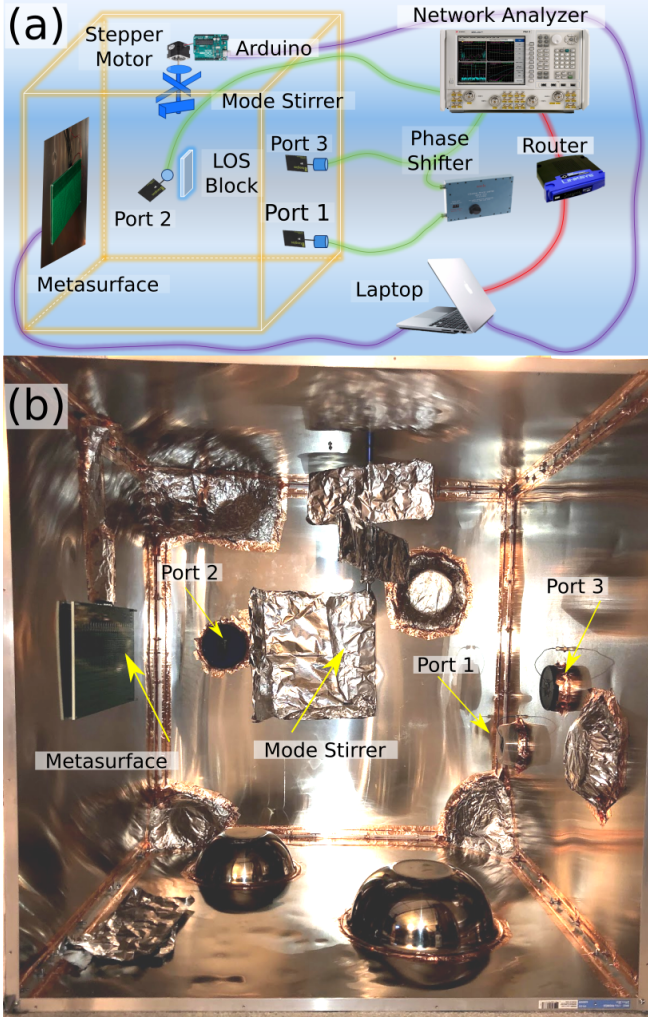


Figure S1. **Cavity configuration.** (a) Experimental schematic of the cavity, showing the metasurface installed on the cavity walls, the locations of the 3 ports, the line-of-sight (LOS) block to prevent direct transmission between Port 2 and Ports 1 and 3, and the mode stirrer that is controlled by a stepper motor through an Arduino. Also shown are the network analyzer, phase shifter, control laptop and router. (b) Photograph of the interior of the cavity showing the components from the schematic as well as the irregular scatters that were installed on the cavity walls.

Pooling layers characterized by the pool size. The output is either the maximum or average value over a sliding window of width given by the pool size. These layers serve to reduce the size of the feature map and help ensure the learning process is position invariant; and 4) Dropout layers characterized by the drop out rate. Dropout layers randomly set the specified percentage of inputs to 0 at each iteration in the training process, providing coarse regularization and simplifying the model.

#### S4. 1D CONVOLUTION

An aspect that is not well understood outside of the signal processing community is how convolutional layers are implemented for inputs containing multiple features. In signal processing, the feature dimensionality is referred to as the number of channels and is sometimes defined as the width or the depth of the data. This arises from color image processing with 3 color channels for red, green, and blue. To perform the convolution over the desired dimension and ensure all the features are captured, the convolution kernel is multidimensional as shown in Fig. S2. For a specified kernel length,  $k$ , the size of the kernel for a 1D convolutional layer with an input containing  $N$  features is  $k \times N$ . The kernel will only be shifted along a single dimension, the local frequency window in our case, but will contain optimized weights for each element. This means that the number of trainable parameters for a 1D convolutional layer scales as  $kN$ , not just  $k$ . For an input data set  $X$ , the output,  $y$ , of the convolutional layer with kernel  $K$  is given by

$$y[n] = \sum_{i=0}^{k-1} \sum_{j=0}^{N-1} K[i, j] X[n - i, j] \quad (\text{S1})$$

For our purposes, we will zero pad the input data by appending  $(k-1)/2$  rows of zeros to either end and keeping the central part of the result, so the number of points along the convolution dimension is constant in the output. By designing a convolutional layer consisting of  $N_l$  filters, there will be  $N_l$  such outputs or new features for the next layer.

#### S5. COMPLEX NETWORK LAYERS AND EXISTING DEEP LEARNING FRAMEWORKS

With complex values, the mechanics of a network layer are the same as for the real-valued counterpart but they incur four times the computational cost due to having both real and imaginary components as well as the cross-terms. Our initial deep learning implementation leveraged Keras [S14] and TensorFlow [S15]. These provide an excellent, high level framework that is very easy to use. Unfortunately this ease of use complicates things when attempting to develop custom complex-valued modules. Complex dense layers are straightforward to implement, but batch normalization, convolution, and recurrent layers are not. While there are repositories with complex deep networks containing some of these modules in Keras [S16] and Caffe [S17], they are not actively maintained and are not formally supported by the frameworks. In the case of Keras, changes to the way the backend is handled in the most recent version (v2.4) mean that the complex library [S16] is no longer functional and would require significant modification to bring up to date.

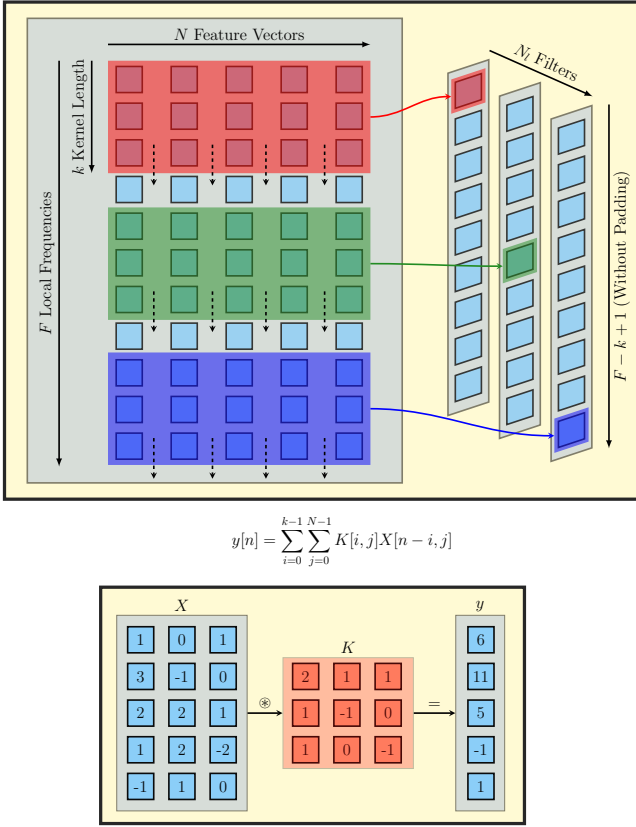


Figure S2. **1D Convolution with Multiple Features.** **Top:** Graphical representation showing the  $N$  feature vectors and  $F$  local frequencies processed by 3 different filters with kernel length  $k$ . The kernel only moves along a single dimension (vertically) even though the data is represented in a 2D format. Each position of the kernel results in a single point in the output vector which has length  $F - k + 1$  if zero padding is not used and length  $F$  if padded as described in the text. The weights for each of the  $kN_i$  elements of the kernel are computed collectively, but can be different. **Bottom:** Numerical example with 3 features containing 5 points each convolved with a kernel of length 3. The input data is zero padded with a row of zeros at the top and bottom and the outputs for the 5 central rows are kept.

This leads us to utilize PyTorch [S18], another deep learning framework. The interface to PyTorch is lower level than Keras, which means it requires more knowledge of Python to use effectively, but that it is also easier to implement custom modules. In addition, there is an open source complex library written by Sebastien Popoff [S19] that includes complex versions of dense, convolutional, and batch normalization layers. We were able to utilize this library with only minor modifications to the batch normalization implementation to handle our multiple feature data sets.

## S6. NETWORK ARCHITECTURE FOR SEQUENTIAL LAYERS

Figure S3 presents the generalized architecture used for sequential layers. The input consists of  $N_i$  feature vectors containing the local 10 MHz windows with  $F$  points in each vector. 1D convolutional neural network (CNN) layers with  $N_l$  filters and a kernel length of  $k_l$  at the  $l^{\text{th}}$  layer perform the feature extraction. As shown in the lower inset, each CNN layer includes a 1D convolution followed by a batch normalization and a rectified linear unit (ReLU) activation function. The batch normalization is used to ensure the distribution of the data (mean and variance) remains relatively constant throughout the network; changing distributions between layers induces internal covariate shift and leads to convergence issues during training [S20]. The ReLU activation function is used in virtually all deep learning networks as it does not experience a vanishing gradient due to saturation, and leads to expedited convergence and generally better solutions than sigmoid like functions [S21].

The CNN layers are grouped together to form stages and are interspersed with 1D max pooling layers defined by the pool size,  $p$ . Also included are dropout layers for regularization, which are not explicitly shown in Fig. S3. The output stage contains a global average pooling layer that averages along the  $F$  dimension, reducing the feature maps to a single dimension. It also converts the complex-valued signals to magnitude and is followed by a dense layer that provides the correct number of outputs,  $N_o$ . As shown in the upper inset, the output of the dense layer is a linear combination of the outputs from the global pooling layer, with a sigmoid activation function used to clip the output between 0 and 1.

## S7. NETWORK TRAINING SETUP

For training the networks, the data was split into 75% training data and 25% validation data. The validation data is used to score the performance after each training run and is not used during the training process itself, so that validation is unbiased. The data was randomly shuffled prior to splitting and each network was trained several times to ensure results were in family and that the training process was unbiased as well.

To score the performance, we need to define metrics for loss and accuracy. The loss function was selected as mean absolute error to emphasize outliers in the data and we define accuracy as the fraction of sets of commands that were predicted without error. To clarify the difference, the loss function is defined as the average of the sum of the absolute value of the true commands,  $T_j$ , subtracted from the predicted commands,  $P_j$ , for set  $j$ , computed over  $N$  sets of  $M$  elements.



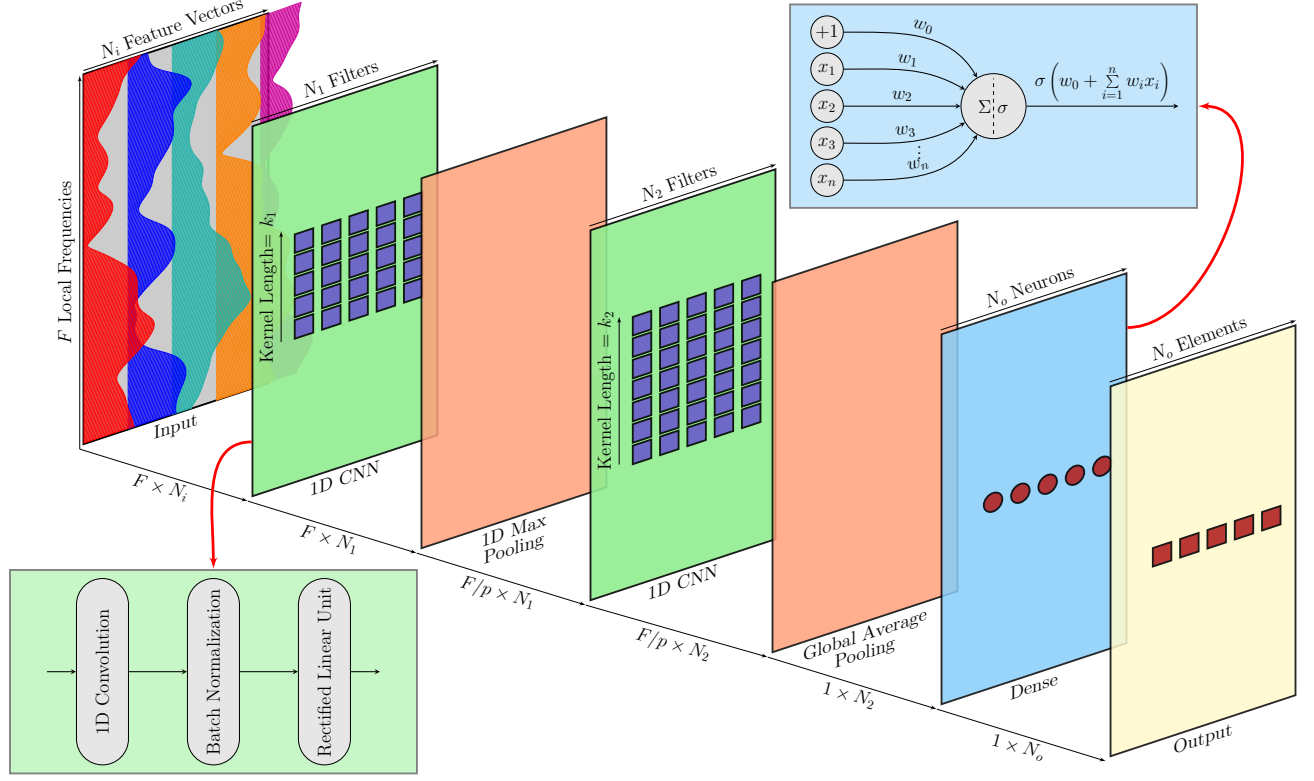


Figure S3. **Sequential network layer architecture.** The input layer consists of  $N_i$  feature vectors containing  $S_{21}$  measurements in a local 10 MHz window of  $F$  points, for a total size of  $F \times N_i$ . This is followed by a series of 1D convolutional layers defined by the number of filters and the kernel length. Each convolutional layer includes a 1D convolution, a batch normalization to keep the distribution statistics constant throughout the network, and a rectified linear unit activation function. Interspersed with the convolutions are 1D max pooling layers defined by the pool size,  $p$ , that serve to reduce the dimensionality of the local frequency window. The output stage consists of a global average pooling layer to further reduce dimensionality and convert the complex-valued signals to magnitude, followed by a dense or fully-connected layer to ensure the correct number of outputs. The dense layer produces outputs that are linear combinations of the outputs from the global average pooling layer, and is followed by a sigmoid activation function to approximate binary values at the output.

$$L = \frac{1}{NM} \sum_j |P_j - T_j| \quad (\text{S2})$$

The loss function is then computed on a per element basis and tells us how close the prediction was on average for each element. The output of the network is floating point rather than binary, so the loss function does not necessarily provide an indication of the total number of incorrect predictions. The accuracy metric is defined as the percentage of sets that were predicted without a single error. It is evaluated on a per set basis and explicitly uses the rounded output (0 or 1) from the network. Because accuracy is computed on a per set basis, it is dependent on the number of elements in a command set and provides a more conservative estimate of performance for the various binning configurations. The loss function is continuous and more appropriate for training where we need to compute a gradient, while accuracy is a better metric for scoring the overall performance.

The networks were trained for 100-200 epochs using

stochastic gradient descent (SGD) with momentum. The basic SGD algorithm has potential problems with pathological curvature, or narrow ravines, which are common around local optima, and the response tends to oscillate back and forth across the ravine. To address this, we can use momentum [S22], effectively forgetting a portion of the previous gradient. Momentum can be thought of as a very coarse approximation of the curvature or 2nd derivative. To accelerate the training, we explicitly use Nesterov momentum [S23].

The networks were trained in batches, meaning multiple data sets were evaluated at each iteration prior to updating the weights. This allows several samples of data to be processed simultaneously so that the effect of changes in the weights are observed over multiple sets of data, improving robustness and desensitizing the response to noise [S24]. A batch size of 100 was used by default.

To prevent the networks from simply training on noise, we introduce an additional regularization step on the loss function. By enforcing an  $\mathcal{L}_2$  regularization scheme, the regularized loss function  $L^*$  is computed from the loss

function  $L$ , and the vector of weights for the current iteration,  $\mathbf{w}_i$ , as  $L^* = L + \lambda \|\mathbf{w}_i\|^2$ . The value  $\lambda$  is referred to as a weight decay. The learning rate,  $\gamma$ , is the step size along the gradient, so the weights are incremented at each iteration as

$$\mathbf{w}_{i+1} = \mathbf{w}_i - \gamma \nabla_{\mathbf{w}_i} L - 2\gamma\lambda\mathbf{w}_i \quad (\text{S3})$$

Finally, the learning rate is stepped down when the loss function plateaus, which allows the network to continue learning when it stalls due to the rate being too high.

### S8. OFFLINE TRAINING RESULTS FOR 5 X 4 BINNING

When using  $5 \times 4$  binning, the metasurface is effectively partitioned into 12 elements, for 4096 possible sets of commands. We measured all 4096 combinations, and the 75%/25% split yielded 3072 sets for training and 1024 sets for validation. The batch size was set to 64 as a result. A purely sequential deep network was utilized, following the layout given in Fig. S3. Four CNN layers, a max pooling layer, and a dropout layer were combined into a stage. Four stages were then used, with the output provided by a global average pooling layer and a dense layer with a sigmoid activation function.

Initial experiments used purely real-valued deep learning layers, in which case the global average pooling layer only provided dimensionality reduction. We were able to establish excellent prediction performance, regularly achieving  $< 10$  total prediction errors over the validation set or  $> 99\%$  accuracy after training for 500 epochs. When switching to complex-valued layers with the same architecture, we were able to regularly achieve perfect prediction (100%) over both the training and validation sets after training for fewer than 100 epochs. This improvement demonstrates that the complex-valued deep learning network is able to exploit phase as well as amplitude to better fit the relationship between metasurface commands and transmitted power.

The training results for the  $5 \times 4$  binning case with complex-valued layers are shown in Fig. S4. Figure S4 (a) shows the loss function evolution for the training and validation sets while Fig. S4 (b) shows the accuracy evolution. The performance is excellent, achieving perfect prediction over both the training and validation data sets. Note that the loss function continues to improve even after the accuracy saturates at 100%. This is because the loss function is continuous and computed using the floating point predicted values rather than the rounded binary values; it shows that the network is still learning and continuing to increase its confidence in the prediction.

### S9. RECEPTIVE FIELD

The receptive field of a CNN defines the number of points in input space that contribute to the result at a single point in a given layer. Our CNNs use zero padding to keep the output size fixed, and the stride and dilation are always set to 1. This means the receptive field at any layer,  $r_l$ , is given by a simple recursive equation dependent on the receptive field at the previous layer,  $r_{l-1}$ , and the kernel length of the current layer,  $k_l$  [S25].

$$r_l = r_{l-1} + k_l - 1 \quad (\text{S4})$$

As shown in Fig. S5, the receptive field for a sequential architecture grows monotonically with depth, with each layer only seeing the receptive field from the preceding layer. An architecture that utilizes parallel branches along with concatenation conserves the intermediate receptive fields, making them available for all subsequent layers and introduces width as well as depth to the network. This is the motivation for the inception module described in the main text.

### S10. OFFLINE TRAINING RESULTS FOR 3 X 3 BINNING

For the  $3 \times 3$  binning configuration, the purely sequential network did not perform very well and was unable to learn the relationships for either the training or validation sets. This inspired the modified inception module that we defined as the Terrapin module in the main paper.

The results for the  $3 \times 3$  binning case with complex-valued layers are shown in Fig. S6. The impact of reducing the learning rate on a plateau can be seen at Epoch 54, where a drop in the learning rate by a factor of 10 induces a drop in the loss function of approximately a factor of 2.

### S11. OFFLINE TRAINING RESULTS FOR 2 X 2 BINNING

For the  $2 \times 2$  configuration with 4000 sets of data, we were able to achieve  $> 98\%$  accuracy on the training set, but were limited to  $\sim 50\%$  accuracy on the validation set. The discrepancy between training and validation results is a hallmark of overtraining. In this particular case, the validation results were improving but stalled as the training results approached 100% accuracy. The error landscape became extremely small with a negligible gradient, so there was no direction to take and continue learning. The network therefore learned specific features of the training set rather than general features of the full range of possible responses. This suggests the overtraining is due to having a limited amount of data (only

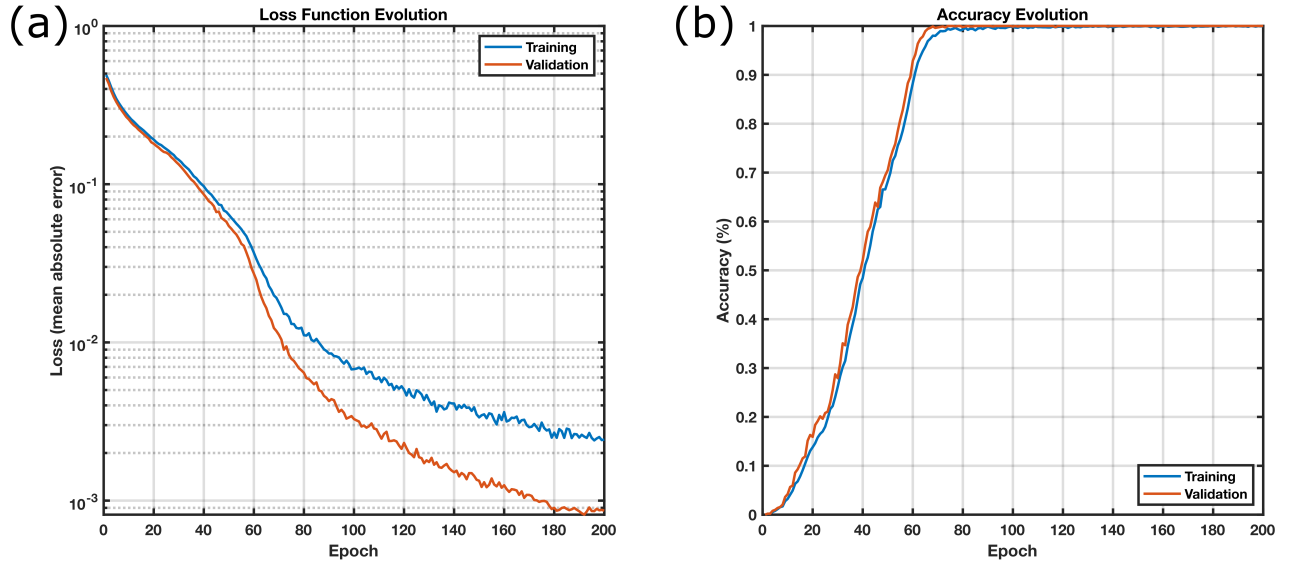


Figure S4. **Deep learning performance with complex-valued layers for 5x4 Binning.** (a) Evolution of the loss function for the training and validation sets over 200 epochs. The loss function measures the average prediction error per element and provides an estimate of the confidence in the prediction. (b) Evolution of the accuracy for the training and validation sets over 200 epochs. Accuracy provides the relative number of sets of commands that were predicted without error, and shows that perfect prediction was achieved on both the training and validation sets in less than 100 epochs. The loss function continues decreasing after the accuracy saturates at 100% because it is continuous and evaluated on the floating point predicted values and the decrease indicates the network is still learning and improving its estimate.

4000 sets). We captured a larger amount of data (10,000 sets) and were able to achieve >95% accuracy on both the training and validation sets. Perfect accuracy for the validation set may be possible with the collection of an even larger amount of data.

## S12. SCATTERING FIDELITY LOSS

Figure S7 shows the decay in scattering fidelity for on-line validation at the 4, 5, and 9 day marks. The accuracy

is still >85% after 5 days, but the number of sets with more than 1 prediction error has increased. After 9 days, the accuracy drops to 65.5% and many cases with 2, 3, and even 4 prediction errors are found.

- 
- [S1] D. A. Hill, *Electromagnetic Fields in Cavities, Deterministic and Statistical Theories*, IEEE Press Series on Electromagnetic Wave Theory (Wiley, Hoboken, N.J, 2009).
  - [S2] B. W. Frazier, T. M. Antonsen, S. M. Anlage, and E. Ott, Wavefront shaping with a tunable metasurface: Creating cold spots and coherent perfect absorption at arbitrary frequencies, *Phys. Rev. Research* **2**, 043422 (2020).
  - [S3] S. Hemmady, X. Zheng, T. M. Antonsen, E. Ott, and S. M. Anlage, Universal statistics of the scattering coefficient of chaotic microwave cavities, *Physical Review E* **71**, 056215 (2005).
  - [S4] S. Hemmady, X. Zheng, J. Hart, T. M. Antonsen, E. Ott, and S. M. Anlage, Universal properties of two-port scattering, impedance, and admittance matrices of wave-chaotic systems, *Physical Review E* **74**, 036213 (2006).
  - [S5] S. M. Popoff, G. Lerosey, R. Carminati, M. Fink, A. C. Boccara, and S. Gigan, Measuring the Transmission Matrix in Optics: An Approach to the Study and Control of Light Propagation in Disordered Media, *Physical Review Letters* **104**, 100601 (2010).
  - [S6] P. del Hougne, B. Rajaei, L. Daudet, and G. Lerosey, Intensity-only measurement of partially uncontrollable transmission matrix: demonstration with wave-field shaping in a microwave cavity, *Optics Express* **24**, 18631 (2016).
  - [S7] Y. Bengio, Deep Learning of Representations for Unsupervised and Transfer Learning, *Proceedings of Machine Learning Research* **27**, 17 (2012).

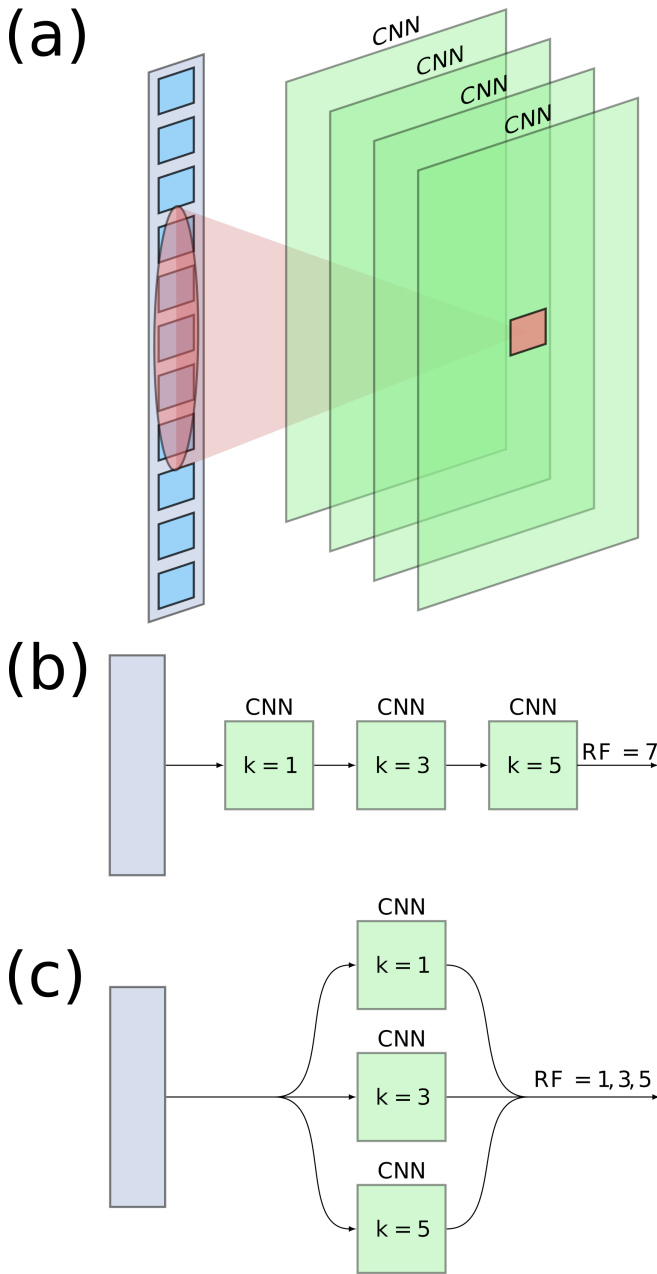


Figure S5. **Receptive Field.** (a) The receptive field of a convolutional neural network (CNN) layer indicates the number of points in input space that contribute to a single point at a given layer. (b) For a purely sequential architecture, the receptive field increases monotonically. (c) A parallel architecture with concatenation produces multiple receptive fields with each available for subsequent layers, promoting sparsity in the representations.

- [S8] Y. Bengio, Deep Learning of Representations: Looking Forward, [arXiv:1305.0445 \[cs\]](https://arxiv.org/abs/1305.0445) (2013).
- [S9] G. F. Montufar, R. Pascanu, K. Cho, and Y. Bengio, On the number of linear regions of deep neural networks, in *Advances in Neural Information Processing Systems*, Vol. 27, edited by Z. Ghahramani, M. Welling, C. Cortes, N. Lawrence, and K. Q. Weinberger (Curran

- Associates, Inc., 2014) pp. 2924–2932.
- [S10] K. Simonyan and A. Zisserman, Very Deep Convolutional Networks for Large-Scale Image Recognition, [arXiv:1409.1556 \[cs\]](https://arxiv.org/abs/1409.1556) (2015).
- [S11] M. Raghu, B. Poole, J. Kleinberg, S. Ganguli, and J. Sohl-Dickstein, On the expressive power of deep neural networks, in *Proceedings of the 34th International Conference on Machine Learning*, Proceedings of Machine Learning Research, Vol. 70, edited by D. Precup and Y. W. Teh (PMLR, International Convention Centre, Sydney, Australia, 2017) pp. 2847–2854.
- [S12] T. J. Sejnowski, The unreasonable effectiveness of deep learning in artificial intelligence, *Proceedings of the National Academy of Sciences* **117**, 30033 (2020).
- [S13] D. H. Wolpert and W. G. Macready, No Free Lunch Theorems for Optimization, *IEEE Transactions on Evolutionary Computation* **1**, 16 (1997).
- [S14] F. a. o. Chollet, Keras, <https://github.com/fchollet/keras> (2015).
- [S15] M. Abadi, A. Agarwal, P. Barham, E. Brevdo, Z. Chen, C. Citro, G. S. Corrado, A. Davis, J. Dean, M. Devin, S. Ghemawat, I. Goodfellow, A. Harp, G. Irving, M. Isard, Y. Jia, R. Jozefowicz, L. Kaiser, M. Kudlur, J. Levenberg, D. Mane, R. Monga, S. Moore, D. Murray, C. Olah, M. Schuster, J. Shlens, B. Steiner, I. Sutskever, K. Talwar, P. Tucker, V. Vanhoucke, V. Vasudevan, F. Viegas, O. Vinyals, P. Warden, M. Wattenberg, M. Wicke, Y. Yu, and X. Zheng, TensorFlow: Large-Scale Machine Learning on Heterogeneous Distributed Systems, [arXiv:1603.04467 \[cs\]](https://arxiv.org/abs/1603.04467) (2016).
- [S16] C. Trabelsi, Deep complex networks, [https://github.com/ChihebTrabelsi/deep\\_complex\\_networks](https://github.com/ChihebTrabelsi/deep_complex_networks) (2018).
- [S17] P. Virtue, Complex caffe, <https://github.com/pvirtue/caffe/tree/complex> (2018).
- [S18] A. Paszke, S. Gross, F. Massa, A. Lerer, J. Bradbury, G. Chanan, T. Killeen, Z. Lin, N. Gimelshein, L. Antiga, A. Desmaison, A. Kopf, E. Yang, Z. DeVito, M. Raison, A. Tejani, S. Chilamkurthy, B. Steiner, L. Fang, J. Bai, and S. Chintala, Pytorch: An imperative style, high-performance deep learning library, in *Advances in Neural Information Processing Systems 32*, edited by H. Wallach, H. Larochelle, A. Beygelzimer, F. d'Alché-Buc, E. Fox, and R. Garnett (Curran Associates, Inc., 2019) pp. 8024–8035.
- [S19] S. Popoff, complexpytorch, <https://github.com/wavefrontshaping/complexPyTorch> (2019).
- [S20] S. Ioffe and C. Szegedy, Batch Normalization: Accelerating Deep Network Training by Reducing Internal Covariate Shift, *Proceedings of the 32nd International Conference on Machine Learning*, PMLR **37**, 448 (2015).
- [S21] K. He, X. Zhang, S. Ren, and J. Sun, Delving deep into rectifiers: Surpassing human-level performance on imagenet classification, in *2015 IEEE International Conference on Computer Vision (ICCV)* (2015) pp. 1026–1034.
- [S22] I. Sutskever, J. Martens, G. Dahl, and G. Hinton, On the importance of initialization and momentum in deep learning, in *Proceedings of the 30th International Conference on Machine Learning*, Proceedings of Machine Learning Research, Vol. 28, edited by S. Dasgupta and D. McAllester (PMLR, Atlanta, Georgia, USA, 2013) pp. 1139–1147.



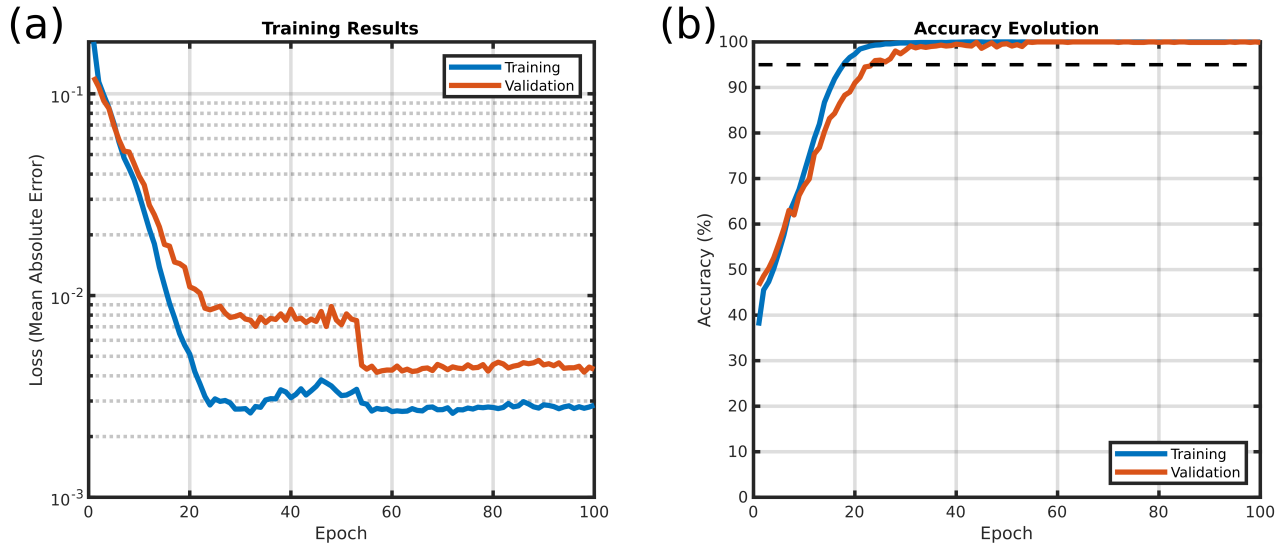


Figure S6. **Deep learning performance with complex-valued layers for 3x3 Binning.** (a) Evolution of the loss function for the training and validation sets over 100 epochs. The loss function hits a plateau at approximately Epoch 33 but shows an additional drop at Epoch 54 when the learning rate is reduced. (b) Evolution of the accuracy for the training and validation sets over 100 epochs. Accuracy provides the relative number of sets of commands that were predicted without error, and shows that perfect prediction was achieved on both the training and validation sets in less than 100 epochs. The loss function continues decreasing after the accuracy saturates at 100% because it is continuous and evaluated on the floating point predicted values and the decrease indicates the network is still learning and improving its estimate.

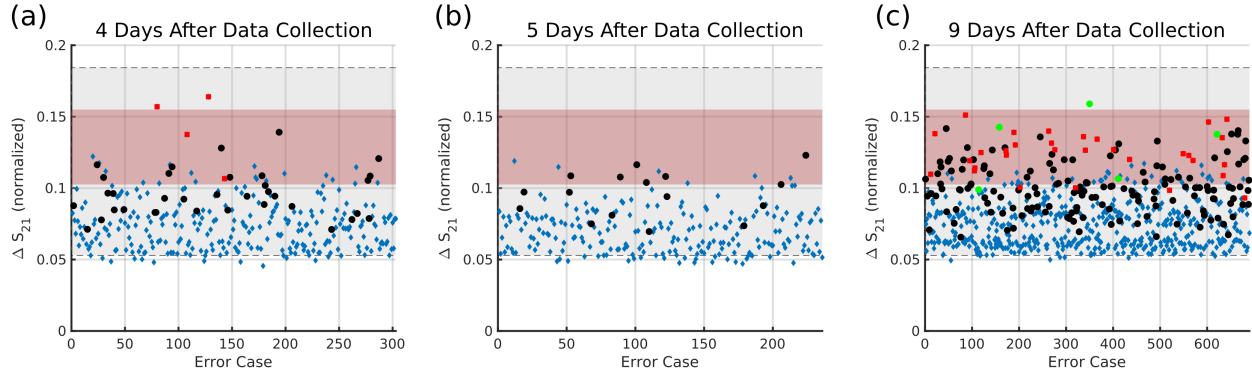


Figure S7. **Scattering fidelity loss over time.**  $\Delta S_{21}$  for online validation sets taken a specified time after the training data was collected. The shaded regions show the extent of the single element Hamming distance results from the training data. The grey region shows the full range from maximum to minimum, and the red region shows the 25<sup>th</sup> and 75<sup>th</sup> percentiles. The blue diamonds indicate cases with a single prediction error, the black circles indicate cases with 2 prediction errors, the red squares indicate cases with 3 prediction errors, and the green circles indicate cases with 4 prediction errors. These panels show that the  $\Delta S_{21}$  for prediction errors is very small, and in the lower region of the statistics covered by observed cases with single element Hamming distances. (a) Validation 4 days after collecting training data, 2000 sets of commands were tested with 303 mispredictions for an accuracy of 84.9%. (b) Validation 5 days after collecting training data, 2000 sets of commands were tested with 236 mispredictions for an accuracy of 88.2%. (c) Validation 9 days after collecting training data, 2000 sets of commands were tested with 690 mispredictions for an accuracy of 65.5%.

[S23] Y. Nesterov, A method of solving a convex programming problem with convergence rate  $o(1/k^2)$ , Soviet Mathematics Doklady **27**, 372 (1983).

[S24] L. N. Smith, A disciplined approach to neural network hyper-parameters: Part 1 – learning rate, batch size, momentum, and weight decay, [arXiv:1803.09820](https://arxiv.org/abs/1803.09820) [cs,

stat] (2018).

[S25] A. Araujo, W. Norris, and J. Sim, Computing receptive fields of convolutional neural networks, Distill [10.23915/distill.00021](https://arxiv.org/abs/10.23915/distill.00021) (2019).